Near-field Development of Buoyancy Driven Flows

by

Derek Bond

A Thesis

Submitted to the Faculty

of the

WORCESTER POLYTECHNIC INSTITUTE

in partial fulfillment of the requirements for the

Degree of Master of Science

in

Mechanical Engineering

by

_____

December 2001

APPROVED:

_____

Dr. Hamid Johari, Advisor

_____

Dr. James C. Hermanson, Commitee Member

_____

Dr. David J. Olinger, Commitee Member

_____

Dr. Nikolaos A. Gatsonis, Graduate Commitee Representative

Abstract

The impact of buoyancy on the development of starting flows in the near field was experimentally investigated using the Digital Particle Image Velocimetry and Planar Laser Induced Flourescence techniques. The experiments were conducted by releasing cylindrical columns of fluid into a glass water tank. Two diameters (0.95 and 1.9 cm) and four aspect ratios, ranging from 2 to 8, were examined. The fluid was released by bursting the thin latex membrane that held it in the tube. The buoyant fluid had a density difference of 4.7%. The flow was imaged at 60 Hz up to 7 diameters downstream. For the aspect ratio of 2, the flow developed into a single buoyant vortex ring (BVR), and was compared to a purely momentum driven vortex ring (MVR) generated with the same setup. For the aspect ratios of 4, 6, and 8, the flow was similar to a starting plume, with a vortical cap, followed by a columnar tail. The BVR's diameter grew linearly in space, with a full spreading angle of 18 degrees, while the MVR's diameter remained constant. The BVR started out as an axis touching ring, and transitioned to non-axis touching, opposite of the behavior of the MVR. The total circulation for the BVR was more than twice the amount predicted by the slug flow model, and the impulse grew linearly in time. The impulse of the MVR decayed slightly after the intial growth. The flows began to transition to thermal behavior at downstream distance proportional to the cube root of the initial fluid volume. For all aspect ratios the impulse grew linearly in time. The growth rate was proportional to the initial buoyant force. The circulation generated by the addition of buoyancy was proportional to the square root of the initial buoyant force. Also the addition of buoyancy suppressed the separation of a starting vortex.

Contents

List of Figures

List of Tables

Nomenclature

At	Atwood number
BVR	Buoyancy driven vortex ring
D	Tube diameter
E	Total energy in the flow
F^*	Total buoyant force
g	Acceleration due to gravity
g'	Acceleration of buoyant fluid due to gravity
I	Total impulse of the flow
L	Tube length
L/D	Aspect ratio
MVR	Momentum driven vortex ring
R	Radial distance
R_{vor}	Radius of vortex ring
Re	Reynolds number
Ri	Richardson Number

T Time for the fluid to discharge from the tube

U_e Axial velocity at the centerline of the exit plane

$\bar{U}$ Average exit velocity

U_{max} Peak exit velocity

V Initial fluid volume

z Downstream distance

Γ Circulation

Γ_{tot} Total circulation of one sign within the flow

Γ_{BL} Circulation ejected from the tube boundary layer

ρ_a Ambient fluid density

ρ_o Buoyant fluid density

$\Delta\rho$ Density difference (ρ_o - ρ_a)

ω Vorticity

ω_{max} Peak vorticity

1 Introduction

Buoyancy has many effects on our lives. These range from small scale plumes from candles and cigarettes, through the plumes created by large cooling stations, up to mesoscale flows in the atmosphere. In all these cases, the presence of buoyancy causes a significant change in the behavior of the fluids involved. Due to the wide range of implications of buoyant flows, there has been a considerable amount of research conducted into this phenomena.

1.1   Past Research

Buoyant flows have traditionally been classified into two major categories, thermals and plumes[1]. The fundamental difference is the manner in which fluid is released. In a plume, buoyant fluid is continuously generated or released from a point source. A thermal is the result of the release of a finite volume of fluid. For a buoyant thermal, the fluid is released with little or no initial momentum. The behavior of these two canonical flows has been documented for many different ambient conditions, and theoretical models have been developed for these cases.

For buoyant convective flows in a uniform environment, the primary quantity governing the behavior in the far field is the total buoyant force[1]. Also, experimental evidence has indicated that the flow becomes self similar[1]. By using dimensional arguments, the following relations can be determined:

$$b = \beta z \tag{1.1}$$

$$U = F_o^{\frac{1}{3}} z^{-\frac{1}{3}} F_1 \left(\frac{r}{b} \right) \tag{1.2}$$

$$g' = F_o^{\frac{2}{3}} z^{-\frac{5}{3}} F_2 \left(\frac{r}{b} \right) \tag{1.3}$$

Here z is the axial position, r is the radial position, b is the plume width, U is the axial velocity, F_o is the buoyant force flux, $g' = g\Delta\rho/\rho_o$, and β is the spreading rate. The functions F_1 and F_2 cannot be determined from a simple dimensional analysis. Either more complex models using some assumption about the turbulence in the plume, or experimental data, can be used to determine these functions.

Applying a similar analysis to the development of a thermal results is the following equations[1]:

$$b = \alpha z \tag{1.4}$$

$$U = F_*^{\frac{1}{2}} z^{-1} F_3 \left(\frac{r}{b} \right) \tag{1.5}$$

$$g' = F_* z^{-3} F_4 \left(\frac{r}{b} \right) \tag{1.6}$$

Here α is the spreading rate, and F_* is the initial buoyant force. These relations were verified by Scorer[2]. He also showed that the $U \propto t^{-\frac{1}{2}}$ and $b \propto t^{\frac{1}{2}}$. These relations are equivalent to those shown above, when written in terms of time instead of space. A more general flow than the thermal is the buoyant vortex ring. This is also produced by the release of a finite amount of buoyant fluid, however, the fluid is released with an initial momentum as well. The addition of this initial momentum alters the spreading rate of the resulting flow[1].

A third class of flows, the buoyant starting plume, has also been investigated. In this

case, the flow is generated by suddenly activating a steady source of buoyant fluid. The application of the previously used assumptions has been successfully applied to this case as well[3]. The flow can be modeled as a plume region capped by a thermal-like region. In this case, the thermal is modified by the introduction of buoyant fluid from the following plume, so the relevant plume power-laws apply.

Analogous work has been carried out on purely momentum driven flows in the far-field. For example, the starting jet has been successfully modeled as a steady jet capped by a spheroidal region of enhanced mixing[4], similar to the model used for the starting plume. These models are also based on the self similar nature of the far field flow.

Although there has been a great deal of knowledge gathered about the far field behavior of jet-type flow fields, interest in the near field region has been relatively overlooked. In part this is due to the very complex nature of the flow in the near field due to the source geometry dependence. However, the importance of near field dynamics has received more attention recently. One major reason for understanding the near field dynamics is because much of the noise generated in a jet is produced here[5]. The recent attention can also be attributed to the development of new experimental techniques. Most notably, Digital Particle Image Velocimetry[6] (DPIV), allows the rapid acquisition of multiple planar velocity fields. This is precisely the kind of data needed to understand the complex, unsteady, non-equilibrium flow present in the near field region of jets and plumes.

Some experiments have been conducted to investigate the near-field behavior of starting axisymmetric jets[7]. These experiments have shown that the flow is significantly different from the flow in the far-field of a starting jet. In particular, the flow field is dominated by a starting vortex ring. The growth and motion of this vortex ring dominates the flow field in the first 10 exit diameters. The vortex ring grows up to a certain point, at which it begins to separate from the trailing flow and maintain a relatively constant downstream celerity[4, 7]. This pinching off process has been described in detail by Gharib et al. They have also developed a model that has been able to reliably predict the pinching off behavior[7].

The addition of buoyancy to the starting jet flow adds another source of circulation. In a buoyant jet both the momentum and the buoyancy contribute to the total circulation released. In absence of any initial momentum, the release of a finite volume of fluid evolves into a thermal with constant circulation in the far field[2]. Furthermore, the generation of circulation by a jet can be estimated by a slug flow model[8]. This model can be made even more accurate by using the empirical correction based on the source aspect ratio derived by Didden[9]. On the other hand, the development of circulation in the near field of buoyant flows is not well understood. Also, the near field dynamics associated with the formation and pinch off of the starting vortex ring may be affected with the addition of buoyancy.

Some work has been done to investigate this region. Johari & Gharib[10] investigated the near field region of plumes generated by releasing a finite volume of buoyant fluid of varying aspect ratios. The results indicated that the formation of the starting vortex ring was indeed affected by the presence of buoyancy. However, detailed information on the development of the circulation of the flow, as well as the internal structure was not obtained.

1.2 Current Research

The current experiments were designed to investigate the effect of buoyancy and source geometry on the formation and development of a starting buoyant flow. In particular, it was desired to determine how the addition of buoyancy changes the formation process of the starting vortex. The structure of the flow was examined using Planar Laser Induced Fluorescence (PLIF). The evolution of the integral measures of motion; circulation, impulse, and energy; were examined by using DPIV.

First, a comparison was made between the development of a purely momentum driven vortex ring, and a buoyant vortex ring generated with the same initial fluid geometry. Secondly, the effect of varying the initial fluid geometry was investigated for buoyant flows.

Based on the initial work done by Johari & Gharib, the following questions were posed:

- How does the presence of buoyancy change the development of the starting vortex ring?

- How does the buoyancy change the development of the circulation, impulse, and energy compared to the MVR?

- How does the initial fluid geometry affect the development of the starting vortex ring?

- How do the circulation, impulse, and energy vary with respect to the initial fluid geometry?

2 Experimental Setup

2.1   Apparatus

The experiments were conducted in a 45.4 liter glass tank to allow free optical access. The tank dimensions were 33 cm by 33 cm by 66 cm high. A schematic of the setup is shown in Fig. 2.1. The buoyant fluid was held in a cylindrical Plexiglas tube, enclosed on the top and bottom by thin latex membranes[10]. The tube was positioned in the tank so that the top was more than 5 diameters beneath the free surface in order to limit any effect of the surface on the release of the fluid. A 30 gauge nichrome wire was placed between the tube end and the membrane. The membranes were burst by passing 3 amperes of current through the wire for 0.8 s. The top membrane was burst first, and then any induced motion was allowed to settle prior to bursting the bottom membrane. All the motion of the membrane was completed within one frame, or 0.17 ms. After each experiment, the tube was checked to ensure that the membrane was not blocking any portion of the tube exit.

The experiments were performed using a negatively buoyant fluid released into a uniform density environment. The density difference, $\delta\rho = \rho_o - \rho_a$, between the two fluids used was 4.7%, within the Boussinesq limit. Five tube geometries with different aspect ratios (length (L) to diameter (D) ratio, L/D), were examined. Three had a diameter of D=1.9 cm with aspect ratios L/D=2, 4, and 6. The other two had a diameter of D=0.95 cm and aspect ratios L/D=6 and 8.

In order to allow clear imaging of the flow, fluids with matching refractive indices were used. Here we follow the suggestion of Alahyari and Longmire[11]. The ambient fluid
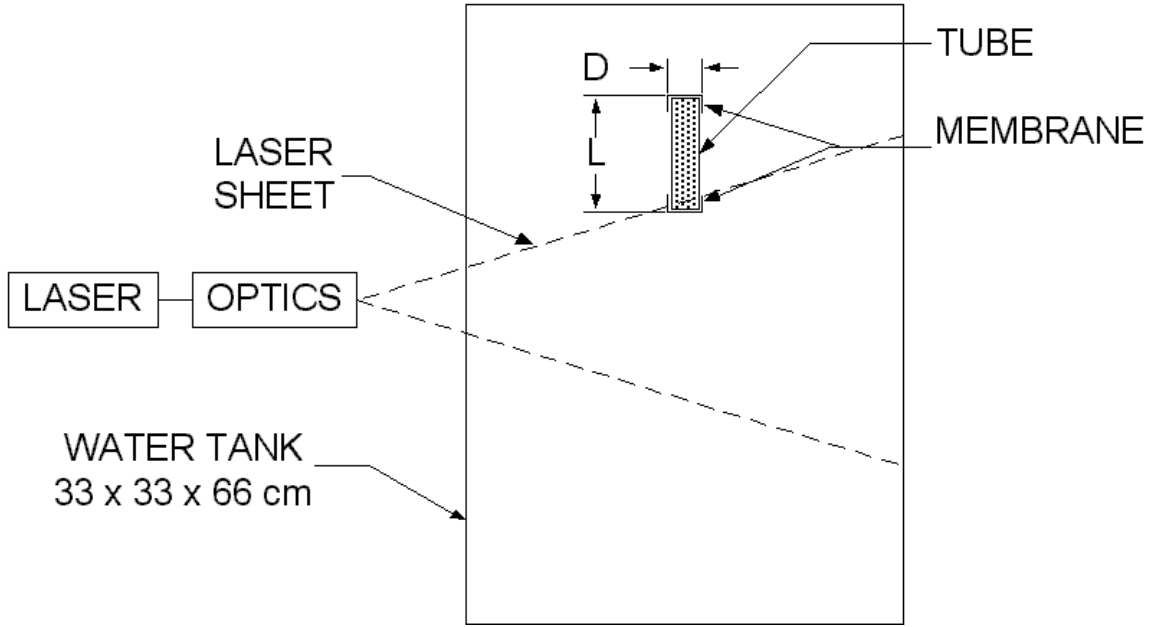
Figure 2.1: Schematic of the Experimental Setup.

was a mixture of glycerol and water, while the buoyant fluid was a solution of potassium dihydrogen phosphate (KH_2PO_4) in water. These chemicals allow a density difference of up to 4.7% to be achieved while maintaining an index match within 0.0002. The tank was periodically refilled in order to maintain a constant density difference and a uniform density environment in the region of interest.

The initial volume, V, for the tubes ranged from 4.1 cm^3 to 32.6 cm^3. With a density difference equal to 4.7% of the ambient density, this corresponds to an initial total buoyant force, $F^* = \Delta \rho g V$ from 1.9×10^{-4} to 1.5×10^{-3} Newtons. The exit velocity, U_e, was obtained from the DPIV data at a point 0.5 D downstream from the tube exit plane. Figure 2.2 shows typical time traces of U_e for each of the aspect ratios examined. Each curve in Fig. 2.2 is marked at the time, T, when the tube had been complete drained. This time was obtained by determining the last video frame where the no ambient fluid was visible between the released fluid and the tube exit. The velocity decreased rapidly after this point in all cases, however, since the tube was open at the top and bottom after discharge, there was a residual induced velocity at the exit plane. Based on simple dimensional arguments
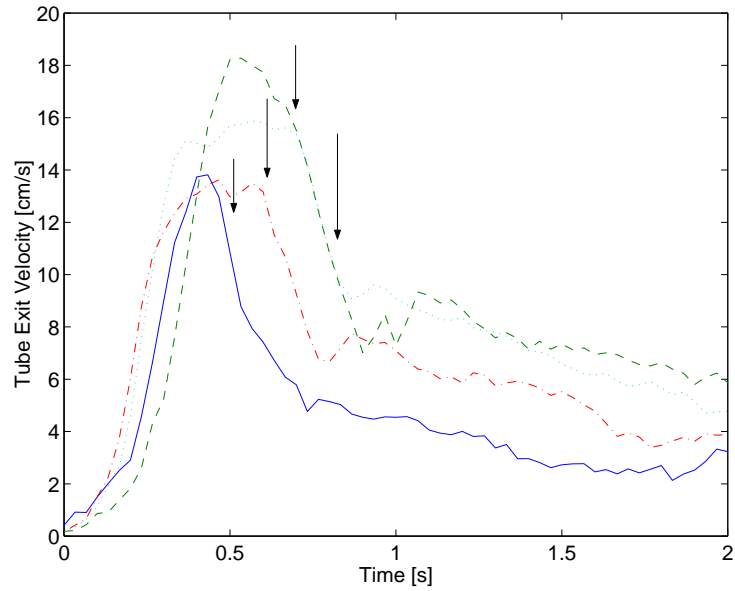
Figure 2.2: Exit velocity as a function of time. The arrows indicate the time that the fluid had completely drained from the tube. Solid line, $L/D = 2$; Dashed line, $L/D = 4$; Dash-dot line, $L/D = 6$; Dotted line, $L/D = 8$

using L, D, gravity (g), and $\frac{\Delta\rho}{\rho_a}$, the time it takes the tube to completely discharge the fluid can be described by Eq. 2.1.

$$T \propto \sqrt{\frac{L}{g'}} f\left(\frac{L}{D}\right) \tag{2.1}$$

For an aspect ratio of $L/D = 2$, the flow accelerated until the tube was empty. A similar trend was seen for the aspect ratio of $L/D = 4$, however, the peak in this case appears to be beginning to flatten. The flattening of the peak is clearly seen in the time traces for the aspect ratios of $L/D = 6$ and 8. The flattening of the peak is due to the viscous effects inside the tube. For the aspect ratios of $L/D = 6$ and 8, the diameter of the tube was smaller, and the boundary layer effects became prominent more quickly.

In order to generate purely momentum driven vortex rings, the setup was modified slightly. The tube was positioned so that the exit plane was just touching the free surface, and the fluid within the tube was being held above the surface by the lower latex membrane. This allowed gravity to drive the fluid even though it had the same density as the ambient

fluid. This setup was used only for an aspect ratio of $L/D = 2$. This setup proved to be fairly sensitive to the positioning of the tube relative to the free surface, as might be expected. This will be seen in Chapter 3 when the MVR is discussed.

2.2 Imaging and Optics

First, a series of experiments using the Planar Laser-Induced Fluorescence (PLIF) technique were performed. Disodium flourescien was added to the buoyant fluid at a molar concentration of approximately 10^{-6}. This ensured that the fluorescence intensity recorded by the CCD camera could be linearly related to the dye concentration. The flow was illuminated from the side of the tank using a thin sheet of laser light produced by a Spectra-Physics argon-ion laser outputting 1.6 W at 488nm. The laser beam was spread into a sheet by an oscillating mirror with a frequency of 1200 Hz. The thickness of the light sheet varied from 1.5 to 2 mm in the region of interest.

The flow was recorded at 60 Hz by a Pulnix 6102 camera. The camera resolution was 640 by 480 pixels, and 300 images were recorded to memory on a PC system via a MuTech MV-1000 frame grabber board. The shutter on the camera was set to 1/125 s in order to minimize the motion during each frame. This was the fastest shutter speed that could be used without the effects from the oscillating mirror. For the PLIF experiments, a Computar zoom lens was used. This lens had a maximum aperture of f1.2, and a focal length of 12.5 to 75 mm. For the experiments, the aperture was set to the lowest practical value of approximately f16 in order to minimize any distortion by the lens.

For the PLIF experiments, the region from the tube exit to approximately 11 diameters downstream was imaged. The resulting in plane resolution was 320 μm for the larger diameter tubes and 180 μm for the smaller diameter tubes. A set of five runs was conducted for each tube.

The next set of experiments was carried out using the Digital Particle Imaging Ve-

locimetry (DPIV) technique. The flow was seeded by 45 micron silver coated hollow glass spheres in both the buoyant and ambient fluids. The flow was illuminated with a frequency doubled dual Nd:Yag laser. The lasers each had a pulse duration of approximately 5 ns. The chosen pulse separation time ranged from 3 ms to 6 ms for the various tubes. The pulse separation time was chosen so that the particle motion in the region of interest was from 5 to 10 pixels. In this case, the laser sheet was created with a cylindrical convex lens with a focal length of 6.35 mm. This created a laser sheet with a spreading angle of 22 degrees[12].

For the DPIV experiments, a Tamron lens was used. This lens had a focal length of 24 mm, and the aperture was set at f16. The camera was not shuttered for these experiments since the laser pulse duration effectively froze the fluid motion for each frame. Since the flow was imaged at 60 Hz, the sampling rate for the velocity field was 30 Hz.

The region from the tube exit to approximately 7 diameters downstream was imaged in the DPIV experiments. Again five runs were performed for each aspect ratio. The images were analyzed by a cross-correlation scheme [6] using 32 by 32 pixel windows spaced 16 by 16 pixels apart. The resulting velocity fields had 29 by 39 vectors. The vorticity was obtained from the velocity fields. The resulting vector spacing was 3.5 mm for the $D = 1.9$ cm tubes and 1.9 mm for the $D = 0.95$ cm tubes.

2.3   Experimental Uncertainty

Although the PLIF data is mostly qualitative in nature, some quantitative measurements were performed on the images. Primarily, the position of the leading edge was determined from the images. In order to obtain this information, the images were thresholded at a chosen level above the background, and the leading edge position was taken to be the most-downstream white pixel in the image. Although the exact position of the leading edge is somewhat subjective, the trends and the extracted celerity are quite reliable.

The leading edge position was generally identified by a steep gradient in the recorded fluorescence intensity. The width of the gradient region was generally 10 pixels. The threshold value was chosen so that the resulting position was near the center of the intensity gradient. This translates to an error of approximately ± 5 pixels or $\pm 0.09D$.

Also, the discharge time, T, was determined from the PLIF images. Since the boundary layers on the tube retard some of the buoyant fluid near the walls, the ambient first became visible near the center of the tube exit. In this region, there was a distinct break visible in the intensity, allowing the time, T, to be determined to ± 0.5 video frames ($\pm 8ms$) for each experiment. There was some variation among the runs, however, the observed time was always within ± 1 video frame ($\pm 17ms$) of the average.

The uncertainty in the DPIV measurements is based on the magnitude of the particle motion. The software used to cross-correlate the images is capable of resolving the particle displacement to within ± 0.01 pixels, however in the interest of maintaining a conservative error estimate, a value of ± 0.05 pixels will be used. The peak particle movements was kept less than 10 pixels, which occurred in the core region of the flow near the exit plane. The average particle motion in the flow region was approximately 4 pixels. This corresponds to an error of 1.25% in the velocity measurements. The vorticity is calculated based on the velocity field, and the method used compounds the error by a factor of 3. Therefore, the error in the vorticity values is approximately 3.75%. It should be noted that these error values are based on an average pixel motion. Near the leading edge of the flow and in the "core" region, the velocities, and therefore the particle motions, were higher; while near the sides and trailing edge of the flow, they were smaller.

Due to the finite size of the experimental facility, the motion and development of the flow may be affected by the presence of walls. The closest walls were the side walls, which were about 15 cm from the regions of peak vorticity in the experiments. The largest measured circulation (see Chapter 4) occurred for an aspect ratio of 4 at about 140 cm^2/s. The effect of an infinite wall on a single vortex core can be estimated using the image

method. The resulting induced velocity is $\Gamma/4\pi a$, where a is the distance to the wall, and Γ is the strength of the vortex. The resulting velocity is 0.7 cm/s. This is the worst case, assuming all the circulation is concentrated at one point. The average velocity measured in the experiments was of the order of 10 cm/s, giving an order of magnitude difference between the average measured quantities and the maximum velocity due to wall effects.

2.4   Dimensionless Scales

As in many problems, the scale of the flow can be important. Due to the buoyant, unsteady nature of the flows examined, choosing the proper scaling parameters can be somewhat difficult. The primary dimensionless numbers of interest for a starting buoyant jet are the Reynolds number, *Re*, and Richardson number, *Ri*. Two velocity scales were used, the average exit velocity, $\bar{U} = L/T$, and the peak exit velocity, U_{max}. The length scale used was D. Also of interest in buoyant flows is the Atwood number, $At = \frac{\Delta\rho}{\rho_o + \rho_a}$. For all these experiments, the Atwood number was 0.023.

	$Re = \frac{UD}{\nu}$		$Ri = \frac{g'D}{U^2}$	
Aspect Ratio	$\bar{U}$	U_{max}	$\bar{U}$	U_{max}
2	1180	2429	1.64	0.39
4	1700	2996	0.79	0.25
6	638	1125	0.70	0.22
8	694	1280	0.59	0.17

Table 2.1: Dimensionless parameters.

Table 2.1 shows the calculated values of *Re* and *Ri* using both velocity scales. The Reynolds numbers indicate that the flow exiting the tube is laminar for aspect ratios of L/D = 6 and 8, and possibly transitional for the aspect ratios of L/D = 2 and 4. However, since the flow is accelerating, it is likely that the flow remains laminar within the tube during the entire discharge period. The Richardson numbers based on the average discharge velocity indicate that the flow ranges from mostly buoyant for the lower aspect ratios to transitional

for the larger aspect ratios[13]. Based on the peak velocities, which occur just prior to T, the flow at the exit plane is strongly influenced by the inertia of the flow, however, these peak velocities decayed rapidly in the region of interest, while the length scales increased. This indicates that the flow in the near field was generally buoyancy-dominated.

3 Buoyant Vortex Rings

For the flows under investigation, there are two major sources of vorticity, and therefore circulation. The first is boundary layer generated vorticity, and the second is baroclinicly generated vorticity. Since the flow is generated inside a tube, boundary layers form on the walls. During the discharge of the fluid from the tube, the boundary layer ejects vorticity into the flow at the tube exit.

$$\frac{\partial \vec{\omega}}{\partial t} + \vec{u} \cdot \nabla \vec{\omega} = \tag{3.1}$$

Baroclinicly generated vorticity is present due to the presence of density and pressure gradients. When the density and pressure gradients in the flow are not aligned, a torque is produced that tends to drive the flow toward an equilibrium position. This generates vorticity at interfaces between two fluids of different densities.

When the ejected fluid has an aspect ratio of less than about 4[7], the flow is expected to develop into a single vortex ring. This is well established for an impulsively started momentum driven vortex ring (MVR). At an aspect ratio of $L/D = 2$, the addition of buoyancy to the flow does not prevent the formation of a vortex ring. However, the behavior of a buoyant vortex ring (BVR) was found to be significantly different from that of a MVR.

In an MVR, the circulation present comes only from the ejection of the boundary layer vorticity. Once the fluid has been released from the tube, there is no longer any circulation being generated in the flow. Since the tube was not closed after the fluid discharge in the current setup (as is typical in vortex ring generators), the induced flow through the tube continued to produce smaller amounts of vorticity in the tube boundary layer. However, the

vortex ring rapidly detached from the vorticity generated by this flow. There is also some opposite sign vorticity ingested from the boundary layer that is induced on the outside of the tube. This opposite signed vorticity was also ingested into the MVR. However, once the fluid has left the tube, the second mechanism of vorticity generation becomes important at the buoyant-ambient fluid interface. This is especially important near the tube exit, where the density and pressure gradients can be at nearly right angles. The effects of buoyancy on the behavior of a vortex ring were studied using a single aspect ratio of $L/D = 2$. The flow structure was qualitatively examined using PLIF. A quantitative investigation was carried out using DPIV.

3.1 Flow Structure

3.1.1 PLIF

Figure 3.1 shows PLIF images of both the buoyant (left) and non-buoyant (right) vortex rings at the point where the fluid has been completely discharged from the tube. It should be noted that based on the DPIV experiments, the shear layer has not separated from the tube for both types of flows at this point. Even at this very early stage in the flow development there is a clear difference between the BVR and MVR. The buoyant flow is in the early stages of rolling up. Also, the front is marked by small mushroom like structures. These structures were observed in all of the buoyant flow cases. The formation of the disturbances on the leading edge are the result of the Rayleigh-Taylor instability at the interface of the buoyant and non-buoyant fluid[14]. The bursting of the latex could possibly have contributed to the development of disturbances on the leading edge of the flow. However, as seen in the non-buoyant case in Fig. 3.1, the disturbance is very weak when buoyant forces are not present. This indicates that the magnitude of any disturbance from the bursting of the latex is small. However, it may initially accelerate the development of the Rayleigh-Taylor instability.
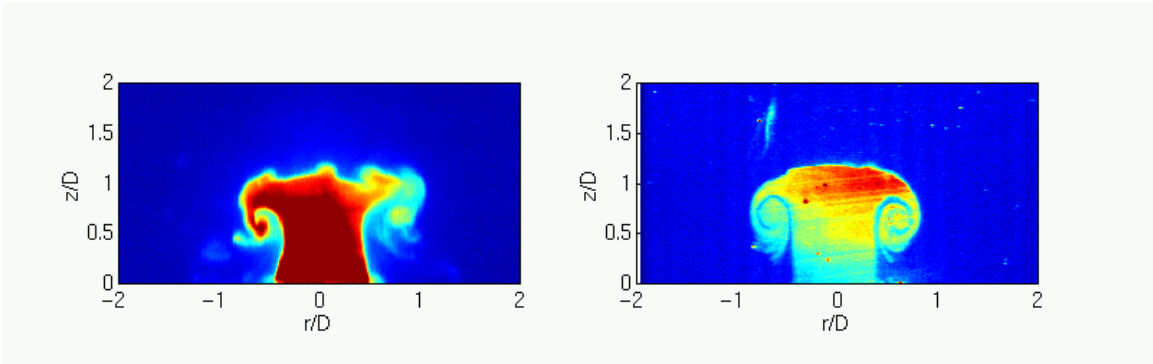
15

Figure 3.1: PLIF images of MVR and BVR just after the vortex ring has been formed. (Note all PLIF images have been inverted from top to bottom and put in false color)

Figure 3.2 shows PLIF images of the BVR and MVR just after they have detached from the generating tube. The MVR appears very similar to the previous image. It is apparent in both cases that there is still a region of fluid that has not yet rolled into the vortex ring structure, however, the shear layer at the edge of this column of fluid has detached from the tube. The BVR is still marked by the Rayleigh-Taylor instability at the leading edge, while the disturbances on the MVR leading edge have not grown visibly. The most significant difference is in the structure of the core region of the vortex rings. The MVR shows the expected rolled up structure. However, only the left side of the BVR has developed into this kind of structure. The initial roll up did not proceed as far in all of the buoyant cases. One of the processes that disturbed the formation of the vortex ring was the propagation of the disturbances from the leading edge into the vortex roll-up region. It was also heavily influenced by the additional vorticity generated by baroclinic torques.

The influence of the buoyant forces can be very clearly seen in the next set of images. Figure 3.3 shows PLIF images of both vortex rings at about $2\,D$. The MVR, on the right, is approximately the same diameter as in the previous images (Figs. 3.1, 3.2), and appears to be a well-formed vortex ring. The BVR on the other hand, has very little indication of structure. The bright regions of buoyant fluid are very likely the "core" of the vortex ring. However, the axial region of the BVR is dominated by ambient fluid. In fact, based on only
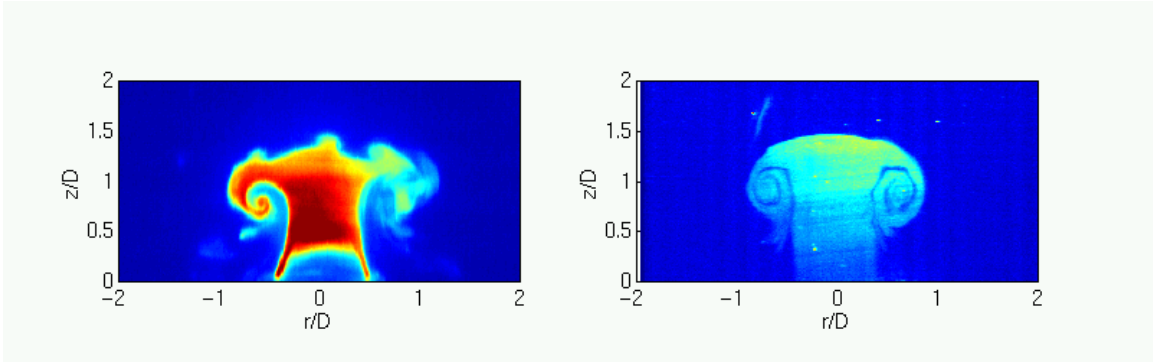
16

Figure 3.2: PLIF images of MVR and BVR after the shear layers have detached from the generating tube.
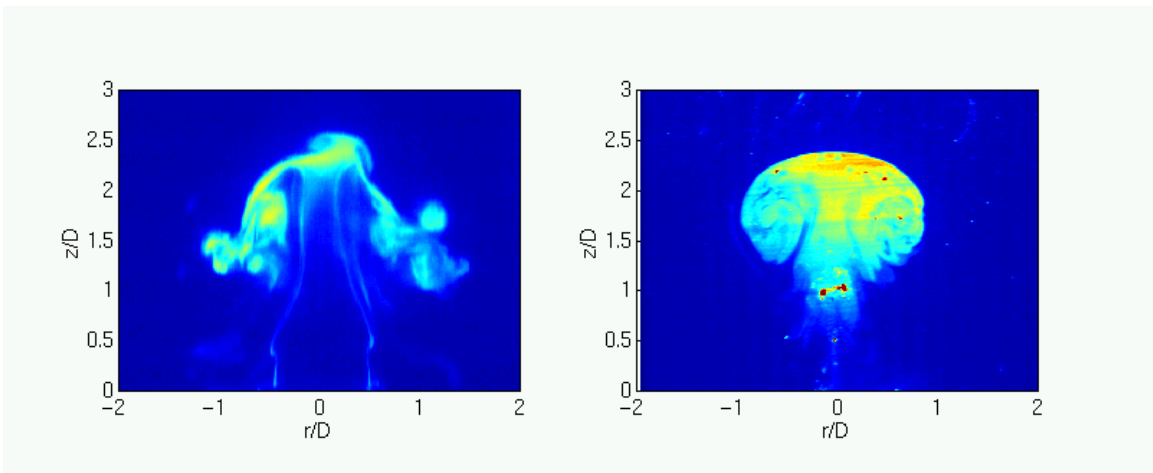

Figure 3.3: PLIF images of MVR and BVR at approximately $2\,D$ downstream.

the PLIF images, it is difficult to describe the buoyant flow as a vortex ring at this point. This rapid entrainment of ambient fluid occurred in the vortex core region as well, resulting in the rapid mixing of the buoyant fluid. Within the region of interest, the recorded image intensity rapidly approached the background image intensity.

The MVR remained very similar as it traveled downstream. Figure 3.4 shows PLIF images of the BVR at 4 and $6\,D$ downstream. At $4\,D$, the bright core regions are approximately $2\,D$ apart. Also, the left side core is much larger than the other. The bright core region persisted until the flow had reached $6\,D$ downstream, and the distance between the cores had grown to be about $3\,D$. The existence of a bright core region was observed in all
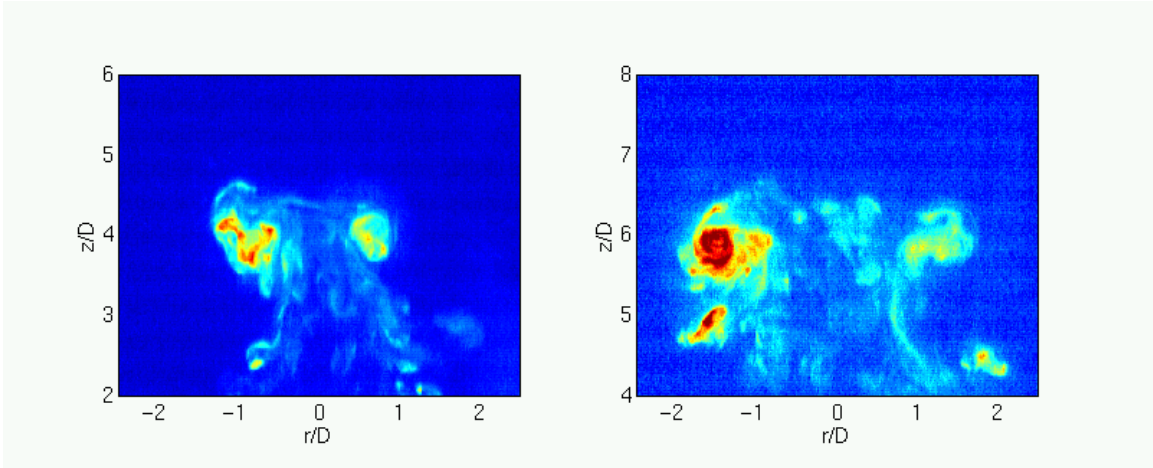
17

Figure 3.4: PLIF images of BVR at 4 and 6 *D* downstream. The color scale has been stretched to improve the contrast.

cases, however, the asymmetry observed in this case was unusual.

3.1.2 Vorticity

The resolution of the PLIF and DPIV techniques used to examine the vortex rings differ by a factor of approximately 16. Due to this difference in resolution, the vorticity fields show very little evidence of the small scale structures seen in the PLIF images.

Vortex rings can be broadly grouped into two classes based on their structure, axis-touching and non axis-touching. In an axis touching vortex ring, the vorticity distribution between the cores monotonically increases (or decreases in the opposite direction) through the origin. Non axis-touching vortex rings contain a region of near zero vorticity in near the axis of symmetry. This is weakly visible in a vorticity contour plot, as will be seen. However, it is easily determined from a graph of the vorticity distribution along a line connecting the two cores.

Figure 3.5 shows the vorticity fields for a BVR and MVR just after the vortex ring had detached from the generating tube. It is clear that there is a "large" scale vortex ring present in the buoyant case. However, even at this early stage of formation, there are significant
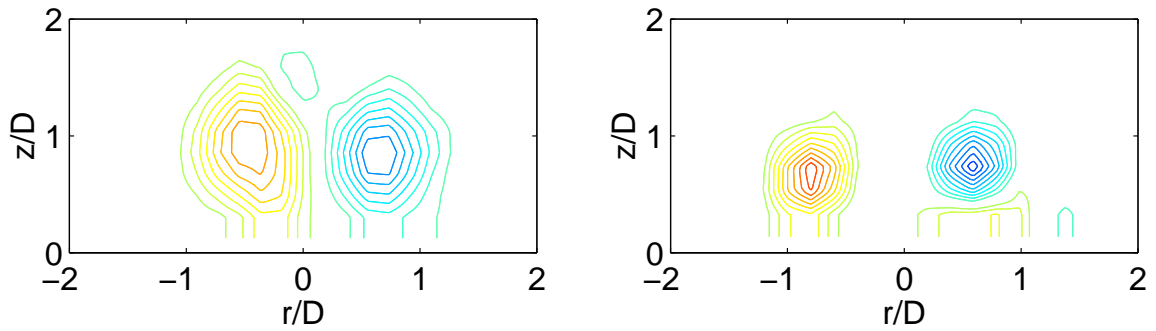
18

Figure 3.5: Vorticity field of MVR and BVR just after the vortex ring has been formed. The contours are at intervals of 10% of the peak, with all contours below 0.5 s^{-1} removed.

differences in the structure of the two types of vortex ring. At this point, the BVR has traveled slightly further downstream, and the vorticity is spread over a larger region. The MVR is definitely not axis touching at this point, evident by the large region of low vorticity on the axis, however, it is difficult to tell the nature of the BVR.

Figure 3.6 shows vorticity fields of the BVR and MVR when the cores had traveled 2 D. At this point, both vortex rings are axis touching, but the BVR is more elongated in the streamwise direction. The BVR is also beginning to show signs of radial expansion relative to the MVR. The vortex cores of the BVR are 1.28 D apart, while the cores of the MVR are 1.14 D apart.

At 4 D downstream, shown in Fig. 3.7, the BVR is less elongated in the streamwise direction. Also, the BVR has continued to grow radially. At this point the BVR cores are 1.64 D apart, while the MVR has grown only slightly to 1.28 D. The growth in the BVR has been great enough that the two cores have begun to separate from each other. The radial expansion of the BVR continued to increase as the vortex ring traveled downstream. Figure 3.8 compares the BVR and MVR at 6 D downstream. Here, the BVR diameter has increased to 2.00 D, while the MVR cores have actually moved inward to 1.14 D.
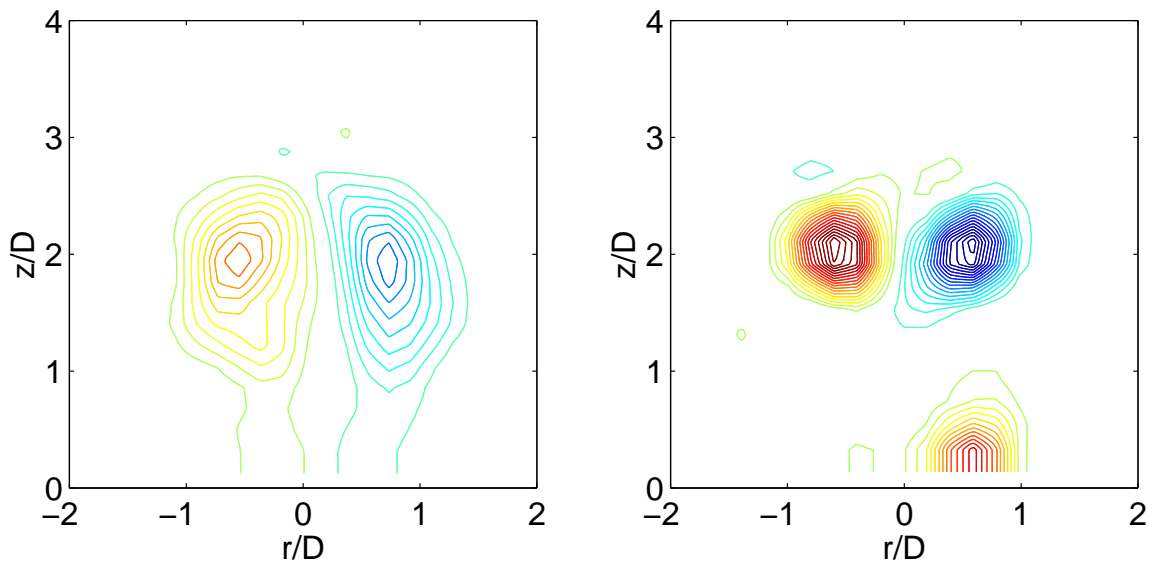
Figure 3.6: Comparison of the momentum and buoyant driven rings at $2\,D$ downstream. The contours are at intervals of 10% of the peak, with all contours below $0.5\,s^{-1}$ removed.
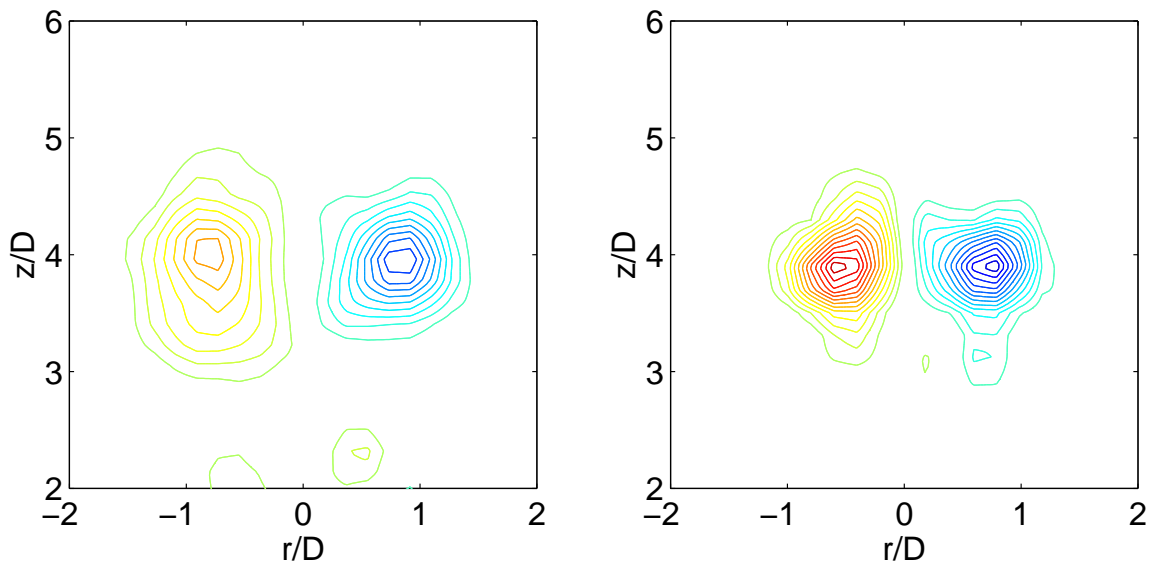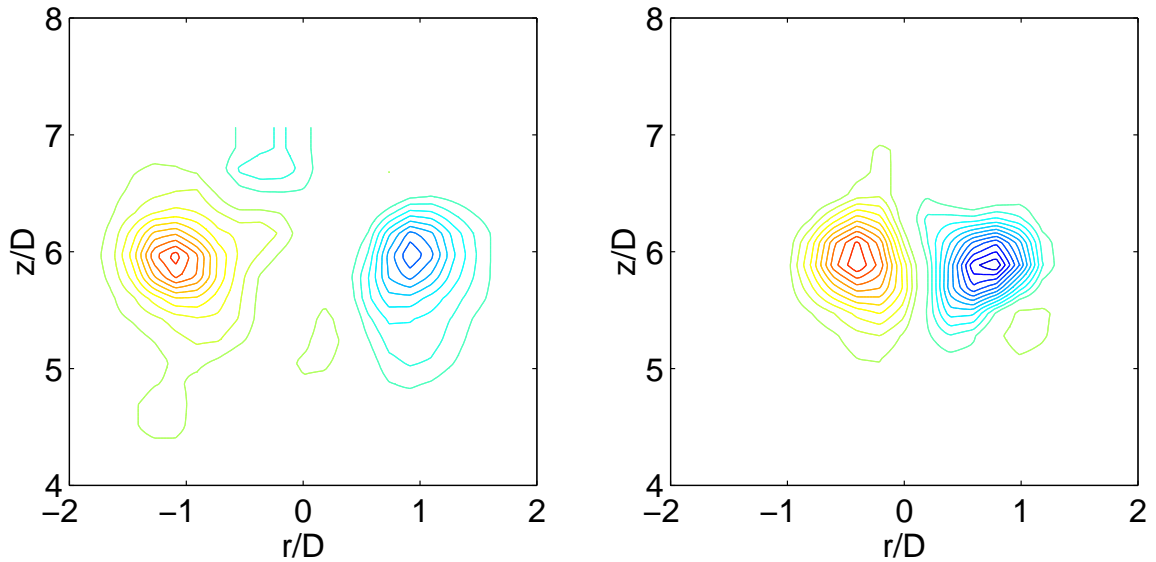

Figure 3.7: Comparison of the momentum and buoyant driven rings at $4\,D$ downstream. The contours are at intervals of 10% of the peak, with all contours below $0.5\,s^{-1}$ removed.

Figure 3.8: Comparison of the momentum and buoyant driven rings at $6\,D$ downstream. The contours are at intervals of 10% of the peak, with all contours below $0.5\,s^{-1}$ removed.

3.2 Vorticity and Velocity Distribution

In order to quantify the differences between an MVR and a BVR, the DPIV data was sampled along a line passing through both vortex cores at several positions. The data was sampled just after the vortex ring was formed, and when the cores had traveled approximately $2\,D$, $4\,D$, and $6\,D$.

Figures 3.9 and 3.10 show the axial and radial velocities for a BVR and MVR respectively. For the BVR, at the point of vortex ring formation, the axial velocity consists of a single broad peak, and there is an outward radial velocity on both sides of the flow. As the flow progressed to $z = 2\,D$, the axial velocity increased, and the flat region near the core was eventually lost. The flow then began to decelerate as seen by the reduced peak at $z = 4\,D$. By the time the BVR had reached $z = 6\,D$ the axial velocity shows a double peak. This is an indication of the spreading of the vortex ring. The MVR develops in the reverse order. At the time the vortex ring separates from the tube, the axial velocity is double peaked indicating that the vortex ring is not axis-touching. This quickly changed, and by $z = 2\,D$,
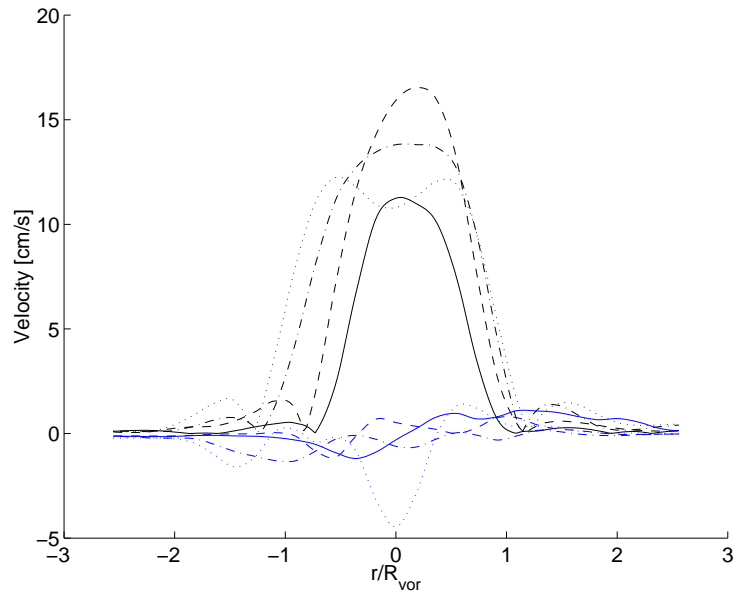
Figure 3.9: BVR axial (black) and radial (blue) velocity distributions along the core. Solid, Ring formation time; Dashed, 2 *D* downstream; Dash-dot, 4 *D* downstream; Dotted, 6 *D* downstream

the vortex ring had a single peak in the axial velocity distribution, indicating that the MVR had evolved from a non-axis-touching to an axis-touching ring.

The structure of the vortex ring is more easily seen from the vorticity distribution along the line passing through the core. The vorticity distribution at each of the downstream positions for the BVR are shown in Fig. 3.11. The vorticity, ω, has been normalized by the peak vorticity, ω_{max}, and the radial coordinate has been normalized by the vortex radius, R_{vor}. The solid line shows the vorticity distribution just after the vortex ring has detached from the tube. It is clearly an axis-touching vortex ring at this point. At $z = 2\ D$, the vortex ring is still axis touching, but the core thickness has begun to decrease relative to the vortex ring radius. By $z = 4\ D$, the vorticity distribution indicates that the vortex ring is becoming non-axis touching. The region near the axis has begun to flatten out. The core thickness relative to the vortex ring size has remained relatively constant. When the vortex ring has traveled $6\ D$, it is clearly not axis touching. There is a region of near zero vorticity separating the two vortex cores.
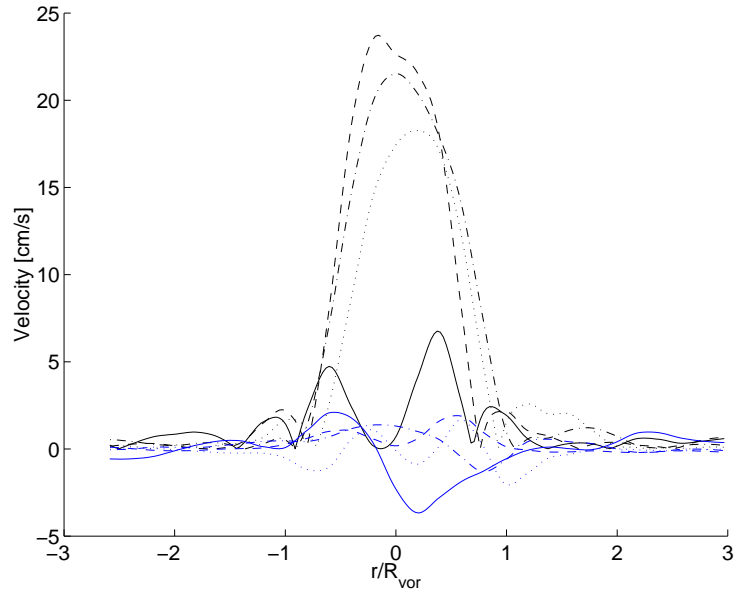
22

Figure 3.10: MVR axial (black) and radial (blue) velocity distributions along the core. Solid, Ring formation time; Dashed, 2 *D* downstream; Dash-dot, 4 *D* downstream; Dotted, 6 *D* downstream

Figure 3.12 shows a similar plot for the MVR. As indicated by the velocity profile, the initial vortex ring that formed at the tube exit was not axis touching. This can be seen by the clear separation of the vorticity between the two vortex cores (solid line). However, at $z = 2$, 4, and 6 *D*, the vorticity distributions clearly indicate that the vortex ring is axis touching, and self similar.

The vorticity distribution in the core region of a vortex ring can often be modelled by a gaussian curve[8]. The core region ($\omega/\omega_{peak} > 0.3$) was fitted with the curve shown in Eq. 3.2, when the radial distance is measure from the peak vorticity location. Figure 3.13 shows a gaussian curve fitted to the self-similar curves of the MVR vorticity distribution. For the MVR, the same curve could be used to fit all of the vorticity distributions after the vortex ring became axis touching.

$$\omega(r) = \omega_{max}e^{-\left(\frac{r}{a}\right)^2} \tag{3.2}$$

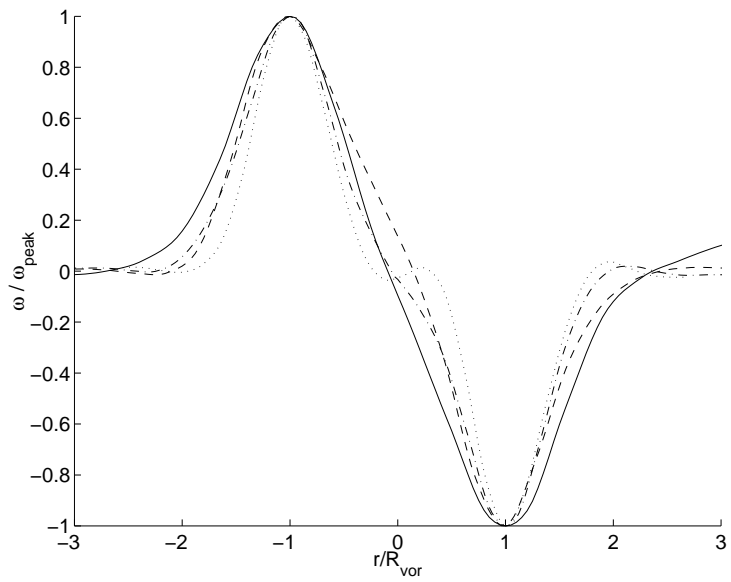The vorticity distribution of the BVR were also gaussian. However, they were not self-

23

Figure 3.11: BVR cross-stream vorticity distribution. Solid, Ring formation time; Dashed, 2 *D* downstream; Dash-dot, 4 *D* downstream; Dotted, 6 *D* downstream
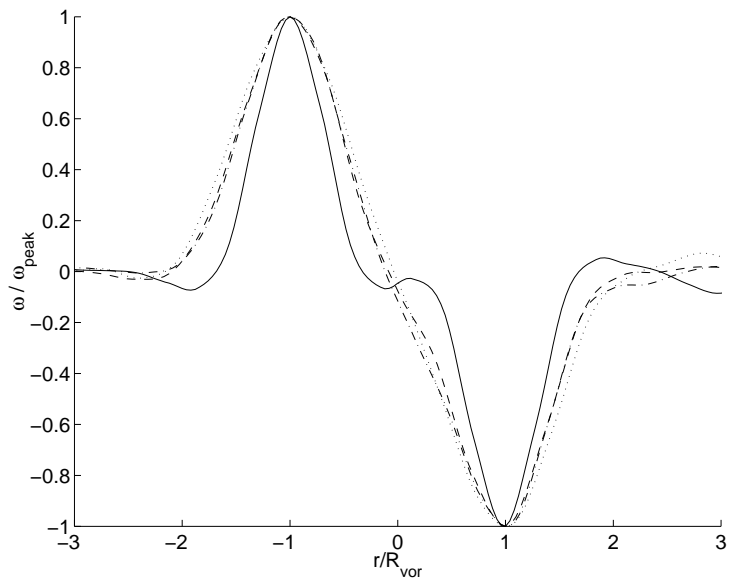

Figure 3.12: MVR cross-stream vorticity distribution. Solid, Ring formation time; Dashed, 2 *D* downstream; Dash-dot, 4 *D* downstream; Dotted, 6 *D* downstream
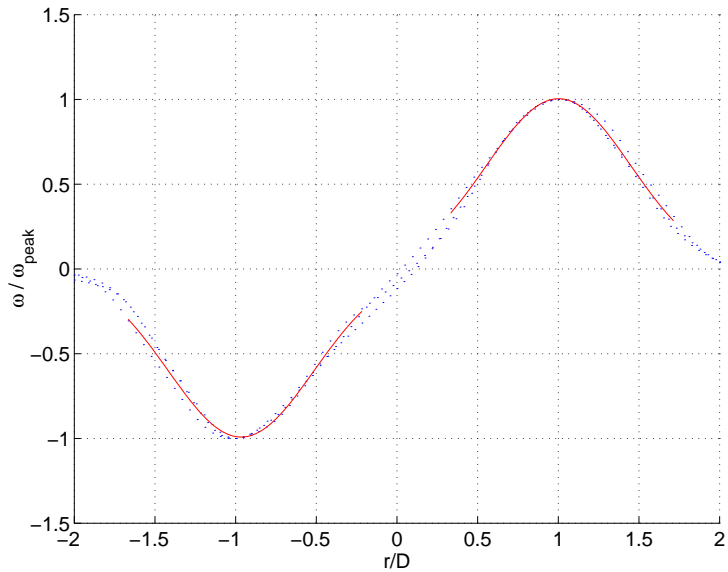
Figure 3.13: Gaussian curve fit to the self-similar vorticity distributions for the MVR.

similar. Figure 3.14 shows a gaussian fit at several times.

The width of the vortex core can be estimated using the curves fitted to the vorticity distributions. The evolution of the width of the vortex core as a function of time was determined by fitting a gaussian curve to the positive and negative peaks of the vorticity distribution for each vorticity field. Figure 3.2 shows the development of the core as a function of time for the BVR. The core size is shown as a fraction of the vortex ring radius. A core size of 1 would be a perfectly axis touching vortex ring. Initially, the BVR is a thick cored vortex ring, with the core being about 70% the size of the vortex ring. As a first order approximation, the BVR linearly transitioned to a non-axis touching vortex ring, with a core size of about 0.3 R_{vor}. However, there are initially some large (20%) oscillations in the core size, indicating the complex nature of the transition process.

On the other hand, the MVR core size was generally thick cored, ranging from about 0.6 to 0.9. There was no clear increasing or decreasing trend for this core size. Figure 3.16 shows the development of the core radius as a function of time for the MVR.
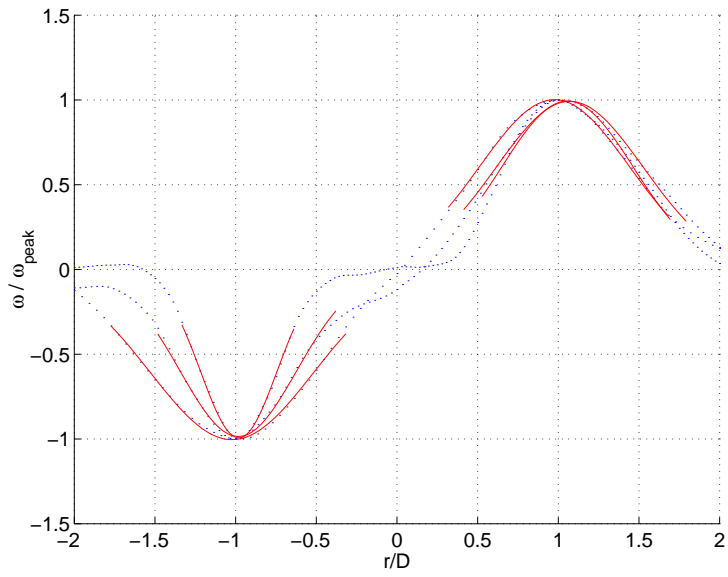
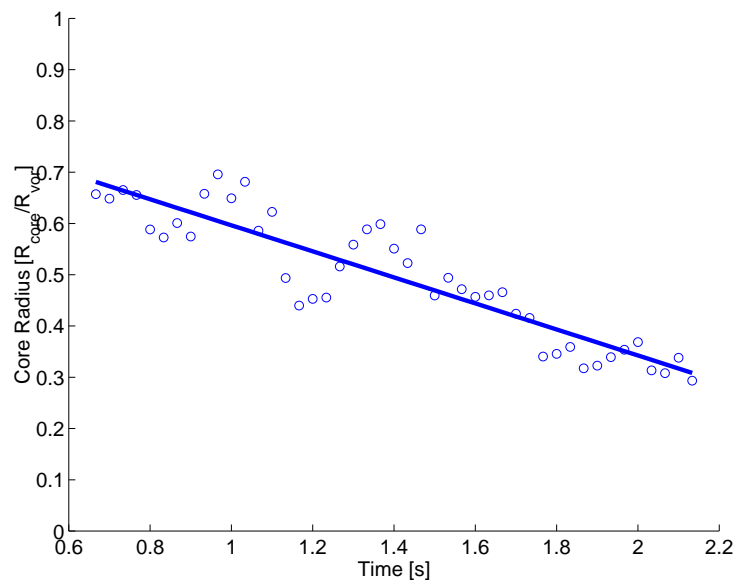Figure 3.14: Gaussian curve fits of the vorticity distribution for the BVR at several times.

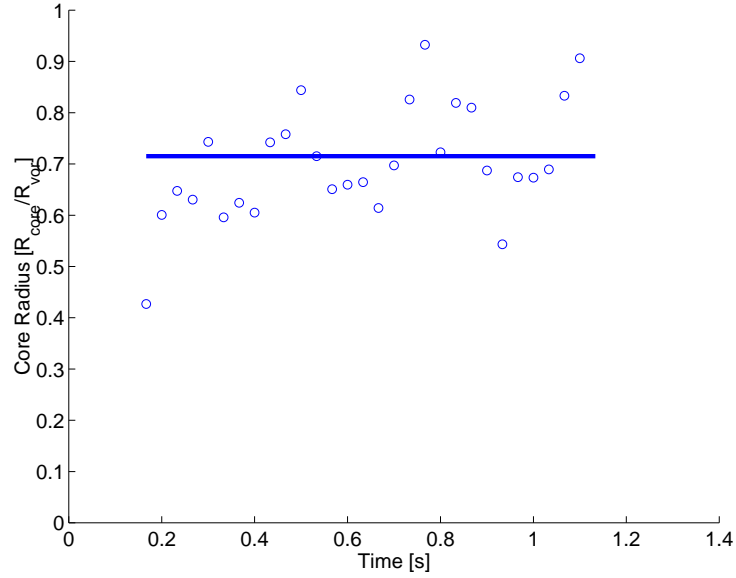Figure 3.15: Development of the relative core size for the BVR.

Figure 3.16: Development of the relative core size for the MVR.

3.3 Integral Measures

The DPIV data were used to compute several integral measures of the flow. The total circulation, Γ_{tot}; impulse, I_{tot}; and energy, E_{tot} were calculated for each half of the flow field. Equations 3.3 to 3.5 show the definitions for each of these quantities. The total circulation is an area integral, while the impulse and energy are volume integrals. The formulations shown are for axisymmetric flow. The domain to be integrated is discussed below.

$$\Gamma_{tot} = \int_D \int \omega \, dr dz \tag{3.3}$$

$$I_{tot} = \pi \int_D \int \omega r^2 \, dr dz \tag{3.4}$$

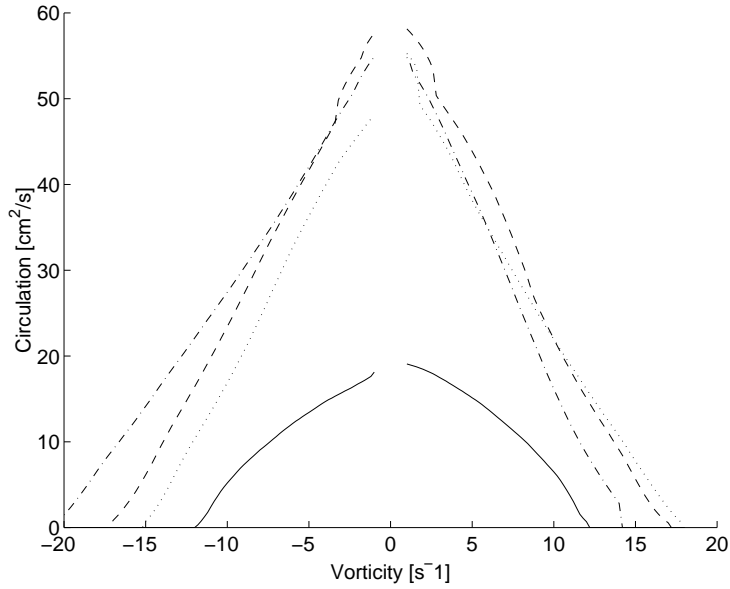$$E_{tot} = \pi \int_D \int \frac{1}{2} |u^2| \, dr dz \tag{3.5}$$

27

Figure 3.17: BVR circulation v. vorticity contour level. Solid, Ring formation time; Dashed, 2 *D* downstream; Dash-dot, 4 *D* downstream; Dotted, 6 *D* downstream

3.3.1 Total Circulation

Although the total circulation can be computed by Eq. 3.3, it can also be computed as a line integral of the velocity along a closed contour, Eq. 3.6. However, this region also needs to be specified. Ideally, the lowest possible iso-vorticity contour should be used. However, the presence of background noise puts a limit on how low the value can be. In the case of a single vortex ring, the total circulation can also be found by two other methods.

$$\Gamma_{tot} = \oint \vec{V} \cdot \vec{dl} \tag{3.6}$$

One procedure, used by Kuzo[15], involves plotting the circulation as a function of the chosen iso-vorticity contour. For these vortex rings, the circulation is a linear function of the vorticity level for $z/D > 2$. This can be seen in Fig. 3.17 and 3.18. This linear dependence, coupled with the assumption of circular vorticity contours, implies the gaussian vorticity distribution seen previously. The total circulation of the vortex ring can be estimated as the intercept of the linear region of this curve with the $0 \; s^{-1}$ vorticity line.
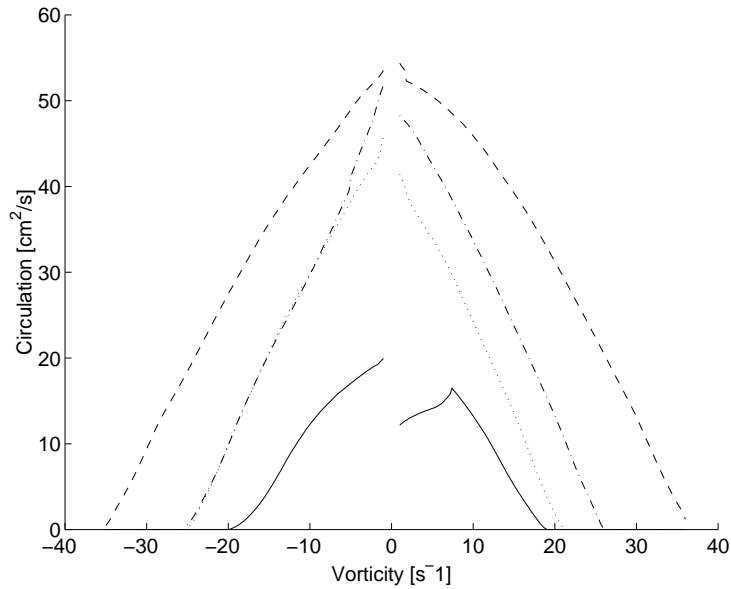
Figure 3.18: MVR circulation v. vorticity contour level. Solid, Ring formation time; Dashed, 2 *D* downstream; Dash-dot, 4 *D* downstream; Dotted, 6 *D* downstream

| | Iso-Vorticity Contour | | | | | |
Run	$0.4\ s^{-1}$	$0.6\ s^{-1}$	$0.8\ s^{-1}$	$1.0\ s^{-1}$	Linear Fit	Circular Contours
1	77.4	69.5	64.3	59.7	59.0	48.8
2	71.0	69.3	67.9	66.6	68.2	53.4
3	93.8	91.2	91.1	89.7	91.5	70.0

Table 3.1: Computed circulation values for the MVR.

The other procedure that can be used is to examine the circulation as a function of the radius of concentric circles about the vortex core. The resulting circulation distributions can be seen in Fig. 3.19 and 3.20. The total circulation is estimated as the maximum on the each curve.

In order to evaluate each of the methods for computing the total circulation, each method was used to compute the final circulation for a single vorticity field of the MVR. Table 3.1 shows the results for iso-vorticity contours at $\omega = 0.4$, 0.6, 0.8, and 1.0 s^{-1}; the vorticity intercept method; and the circulation v. radius method.

As expected, the measured circulation value decreases with increasing vorticity level. At the low vorticity levels the data begins to be affected by noise. At this point, the contours
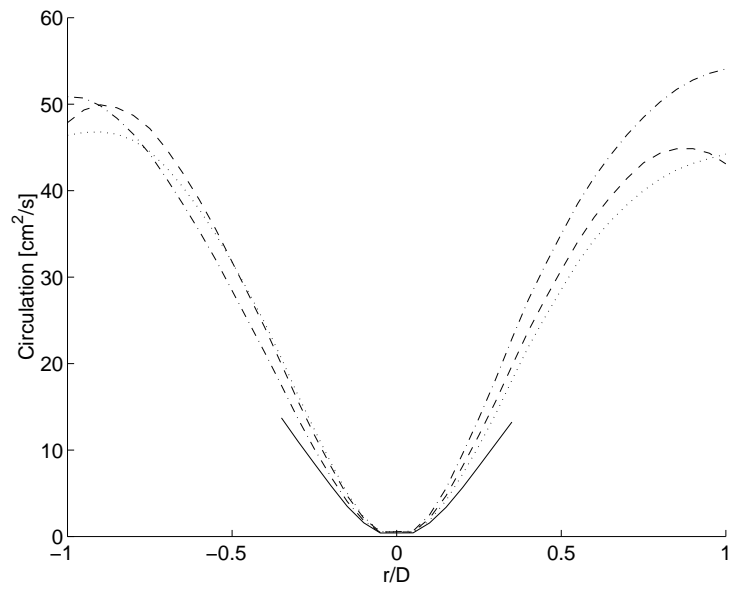
Figure 3.19: BVR properties obtained from DPIV data. Solid, Ring formation time; Dashed, 2 *D* downstream; Dash-dot, 4 *D* downstream; Dotted, 6 *D* downstream
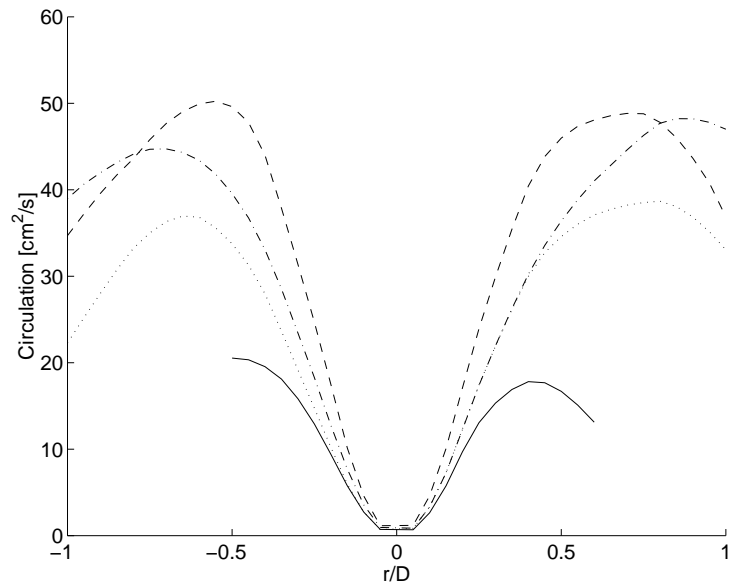

Figure 3.20: MVR properties obtained from DPIV data. Solid, Ring formation time; Dashed, 2 *D* downstream; Dash-dot, 4 *D* downstream; Dotted, 6 *D* downstream

begin to become jagged. However, at a vorticity level of $\omega = 1 \; s^{-1}$, the values compare well with the value predicted by the intercept of the linear fit. Also, since the contours are not circles, the value predicted by the peak of the circular contours is lower than that predicted by the intercept of the linear fit. The values obtained at $1 \; s^{-1}$ are consistently close to the values obtained by the linear fit intercept. This region will be used for determining Γ_{tot}.

Figures 3.21 and 3.22 show the temporal evolution of Γ_{tot} for the BVR and MVR. Here, the most notable feature is the large amount of circulation generated by the presence of buoyancy. The dashed line indicates circulation computed using the slug flow model[8]. The slug flow model estimates the circulation according to Eq. 3.7. However, this model tends to underestimate the circulation, so the correction developed by Didden[9] (Eq. 3.8) was used. The time when the tube has been completely discharged is marked by horizontal and vertical dashed lines, indicating the time, and the total circulation generated in the boundary layers.

$$\Gamma_{SF} = \frac{1}{2} \int_0^T U_e^2 dt \tag{3.7}$$

$$\Gamma_{corr} = (1.14 + \frac{0.32}{L/D})\Gamma_{SF} \tag{3.8}$$

For the MVR, there is insufficient time resolution for this computation to be accurate. Also, the BVR shows a clear leveling off of the total circulation. This is the same behavior observed in thermals[1], even though, as discussed, the BVR is not behaving entirely like a thermal at this point. The transition from rapidly increasing circulation to nearly constant circulation is very abrupt, and there may be a slight decrease in circulation prior to leveling out. This is possibly due to viscous dissipation in the transition.
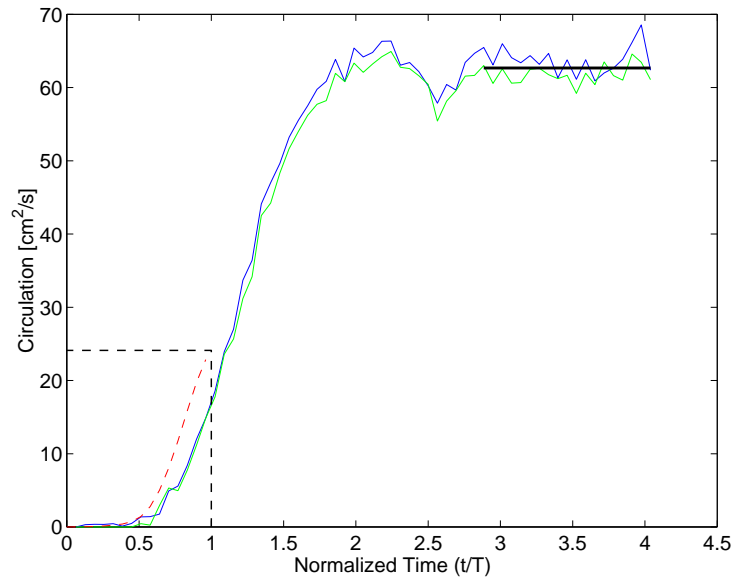
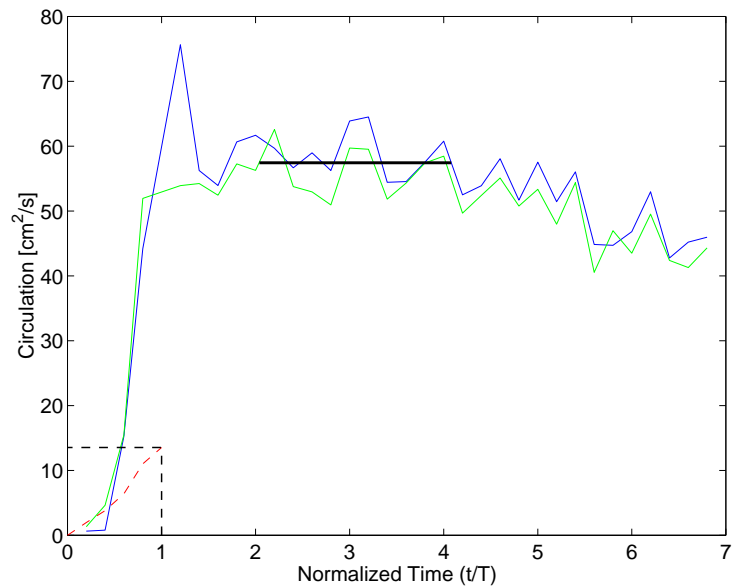Figure 3.21: Circulation development for a buoyant vortex ring.

Figure 3.22: Circulation development for a momentum driven vortex ring.

3.3.2   Impulse

The impulse of the flow, *I*, was calculated using Eq. 3.4. The same contours ($\omega = 1s^{-1}$) used to compute the total circulation were used to compute the impulse. The integral was estimated by creating a triangular mesh using the contour points and all the data points inside the contour. The value of the integral on each triangle was computed as the average of the integrand value at each of the vertices multiplied by the area of the triangle. In order to check the accuracy of the method, the circulation was also computed by numerically integrating the vorticity field. The values obtained were about 2-3 % less than the values obtained from the line integral method.

Figures 3.23 and 3.24 show the development of the impulse with respect to time, averaged over all the runs. Since the flow is assumed axisymmetric, only one half of the flow needed to be included. However, both halves were computed separately to allow a comparison to be made. The impulse of the MVR shows a rapid increase. However, this increase suddenly stops and the impulse appears to begin a slow decline. This would be expected due to viscous dissipation, as well as loss of impulse to vorticity levels lower than $\omega = 1$ s^{-1}. The BVR is a much different story. The impulse follows a linear increase with time throughout the measured time frame. In buoyant flows in the far field, the total buoyant force is the conserved quantity. The linear increase of impulse with respect to time is due to the constant addition of momentum from the force on the buoyant fluid.

3.3.3   Energy

Using the same contour, the energy contained within the flow, E_{tot}, was computed by numerically integrating Eq. 3.5. The same method used to calculate the impulse was employed. Again, the energy was computed separately using each half of the flow. Figure 3.25 shows the development of the energy in the MVR. There is a rapid increase as the vortex ring is formed, followed by an abrupt transition and a steady decrease. Since the ring is moving steadily at this point, the decrease in energy must be due to viscous dissipation.
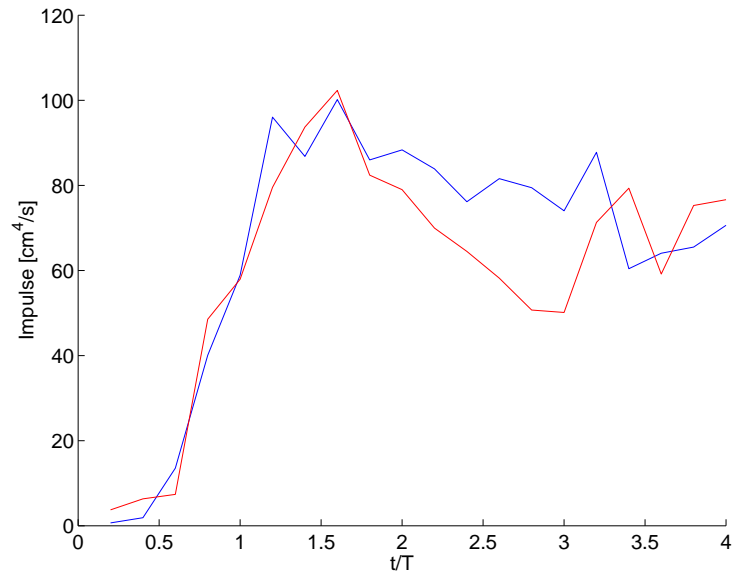
Figure 3.23: Impulse for the MVR integrated in a iso-voriticy contour at $\omega = \pm\ 1\ s^{-1}$.

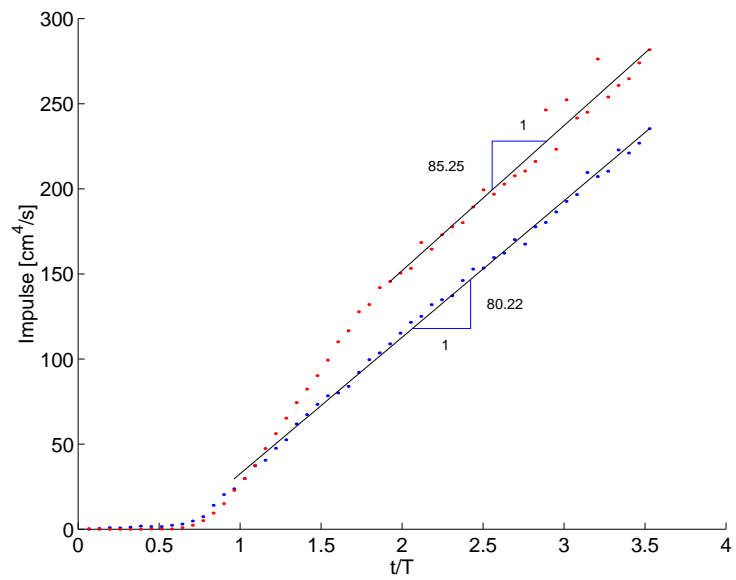
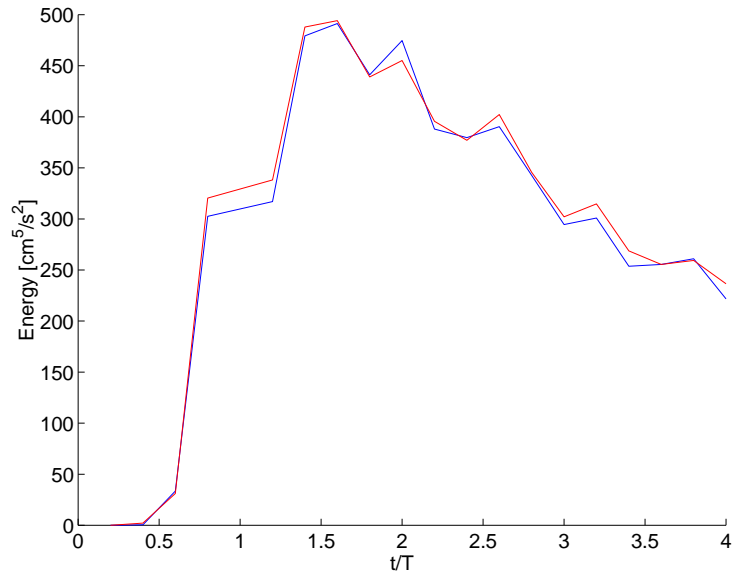Figure 3.24: Impulse for the BVR integrated in a iso-voriticy contour at $\omega = \pm\ 1\ s^{-1}$.

Figure 3.25: Energy for the MVR integrated in a iso-voriticy contour at $\omega = \pm\ 1\ s^{-1}$.

Figure 3.26 shows the development of the energy in a BVR with respect to time. Again there is a rapid increase in the energy initially. Then the energy approaches a steady state value.

3.4   Vortex Core Motion

Although the vortex core location is nearly impossible to determine from the PLIF images for the BVR, the vorticity distribution exhibited a clear peak, which was chosen to identify the vortex core location. The trajectory of this core location was then examined, allowing the determination of the diameter, growth rate, and celerity of the vortex ring.

3.4.1   Axial Motion

Due to the nature of the setup, the MVR velocity was very sensitive to the position of the generating tube. A small change in the vertical tube position had a visible effect on the vortex ring velocity and total circulation. Figure 3.27 shows the downstream position of
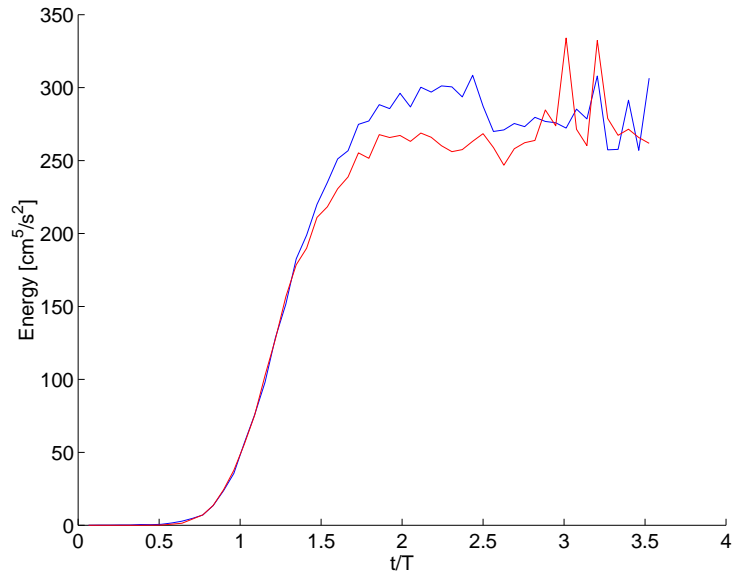
Figure 3.26: Energy for the BVR integrated in a iso-voriticy contour at $\omega = \pm\ 1\ s^{-1}$.

the vortex cores for 3 different MVR runs. The curves are all quite linear, however, the slopes vary due to the effect mentioned above.

The axial motion of the BVR was more consistent. This is because the generating tube was fully submerged, eliminating the problem observed with the MVR. Figure 3.28 shows the average axial motion for the BVR. The most notable difference from the MVR is the initial non-linearity in the motion. There is a brief period of acceleration after the BVR has formed and detached from the tube. This is followed by a deceleration and then a linear region. This linear region corresponds well with the transition region to be discussed in Chapter 4. It is notable that the BVR has not yet begun to behave as a thermal, where a square root dependence would be expected[1, 2, 16].

3.4.2 Radial Motion

The spatial trajectories of the BVR and MVR were very different. Figure 3.29 shows one BVR (triangles) and MVR (circles). Within the first few diameters, the trajectories are very similar. There is a small expansion just downstream from the tube exit plane, followed by
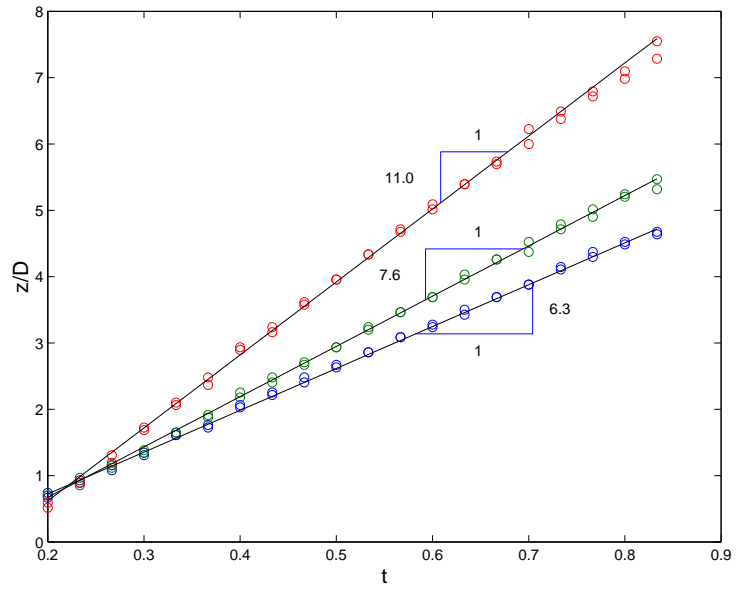
36

Figure 3.27: Axial motion of the MVR for each case. The sensitivity to the tube place can be seen in the variation of the slope.
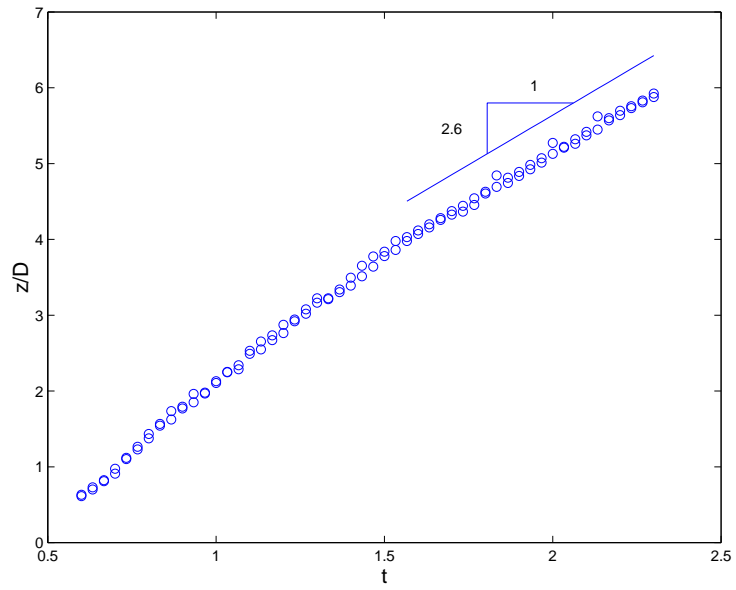

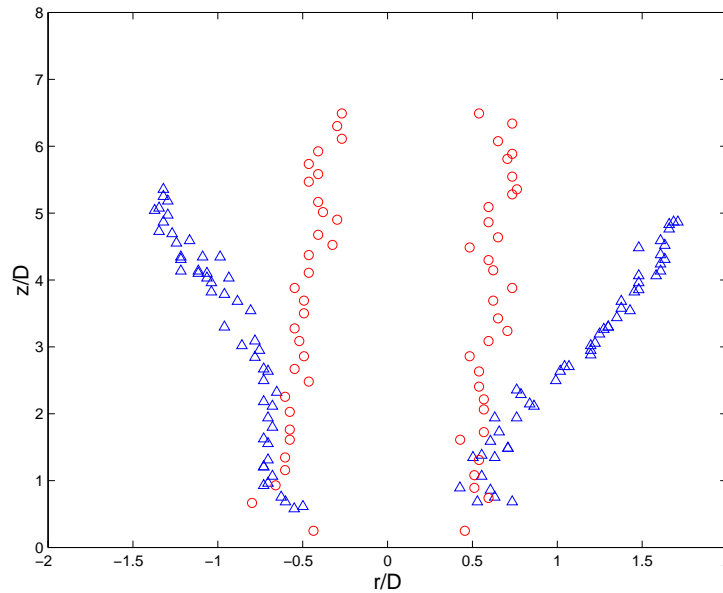Figure 3.28: The average axial motion of all the BVR experiments.

Figure 3.29: Example of vortex core movement for a buoyant and non-buoyant vortex ring. Triangle - BVR; Circle - MVR.

a contraction. However, the BVR suddenly begins to expand near z = 2 *D*. The expansion was not always symmetric, as can be seen in this example. Also, the trajectory of the BVR's were significantly scattered. This can be seen in Fig. 3.30. The MVR trajectories are much more consistent.

The trajectories for each class of vortex ring were averaged to produce a single trajectory. Figure 3.31 shows the results of the averaging process. The average MVR trajectory still shows a small increase in size just downstream of the exit plane, followed by a contraction. The MVR then travels downstream with a nearly constant width. The average BVR trajectory also indicates that the initial ring formation is followed by a slight expansion. The average trajectory shows a very linear growth after about *z* = 1.5 *D*.

In order to compare the growth rate of the BVR with previous far-field growth rates for thermals and buoyant vortex rings, the vortex ring radius was computed as half the distance between the vortex cores. Figure 3.32 shows this diameter as a function of downstream distance for the BVR. There is the initial non-linear region followed by a long linear expansion. The expansion can be fitted with a straight line, and the resulting slope is 0.16.
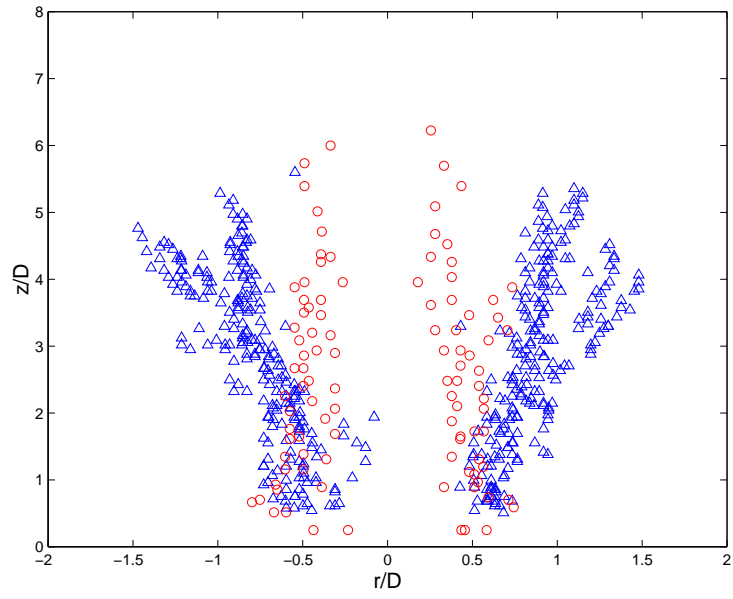
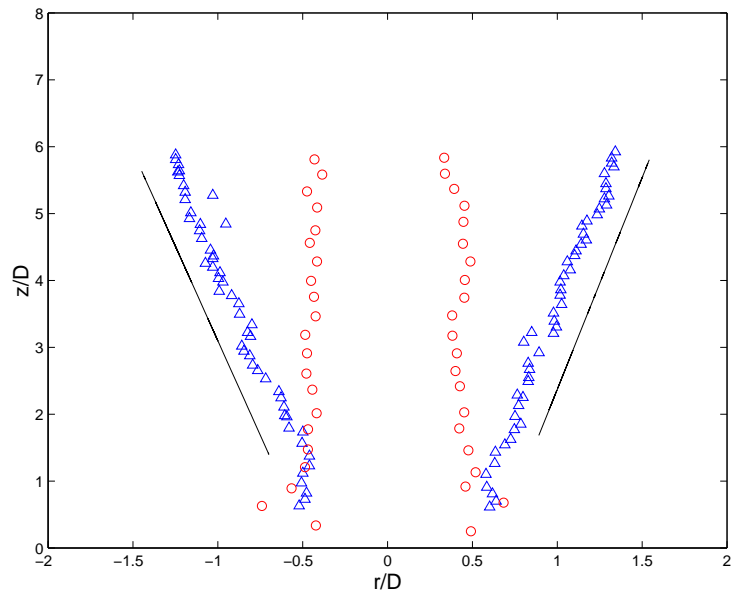Figure 3.30: Vortex core paths for all cases. Triangle - BVR; Circle - MVR.

Figure 3.31: Average vortex core paths for buoyant and non-buoyant vortex rings. Triangle - BVR; Circle - MVR.

The BVR is most accurately described as a buoyant vortex ring, since the circulation was generated both in the tube boundary layer and by the baroclinic torques. Turner[1] showed that the expansion of a buoyant vortex ring in the far field is described by Eq. 3.9.

$$R = \alpha z = \frac{F^*}{2\pi c \Gamma_{BL}^2} z \qquad (3.9)$$

The spreading rate, α, depends on the initial buoyant force, F^*, and the circulation produced in the boundary layers of the generating apparatus, Γ_{BL}. The constant c is related to the exact profile of the self similar profile of the flow in the far field and should be of order one. The experimental results indicate that α is 0.16. The value of Γ_{BL} was computed using the corrected slug flow model described earlier, and the initial buoyant force was computed based on the experimental setup. These values are 25 cm^2/s and 500 cm^4/s^2, respectively. The resulting value for c is approximately 0.8. So, even though the flow has not reached self similarity, as seen by the vorticity distribution, and is not in the far field, this relation is still approximately valid.

The spreading rate, α, for a thermal in the far-field has been experimentally determined to be approximately 0.25[2, 16] or 15 degrees, while it is reduced for buoyant plumes[16] to about 0.2, or 11 degrees. However, these spreading rates are based on the visible exterior boundary of the flow, while the measured spreading rate above is based on the position of the vortex core. This may be the primary source of the difference.
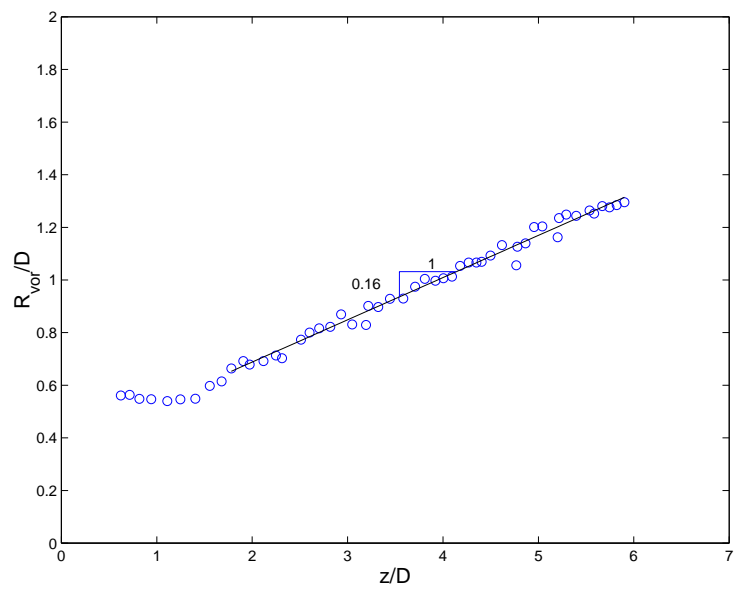
Figure 3.32: Average radius of the BVR.

4 Buoyant Starting Flows

The initial goal of these experiments was to examine the effects of the released fluid geometry, i.e. aspect ratio, on the subsequent development of the flow field. In particular, whether the initial vortex ring formation was affected by the addition of buoyancy. Both the PLIF and DPIV techniques were used for each of the geometries examined. Although PLIF can be used to determine concentration values, due to the strong reflection of the incident laser light near the tube exit, the results were constrained to primarily qualitative information about the flow structure.

4.1   Flow Visualization

The evolution of the release of a finite parcel of buoyant fluid can be divided into two phases for the range of L/D examined. During the first phase, the buoyant flow emerging from the tube accelerated and rolled up into a starting vortex ring. During this phase, the fluid completely discharged from the tube. This was followed by a transition period after which the released parcels began to decelerate. The final phase consisted of a decelerating fluid mass similar to a thermal. The exact timing of when each phase began and ended varied with the released fluid aspect ratio.

A series of PLIF images are shown in Figs. 4.1 to 4.4. The images have been assigned false color. The time step between the images in each figure is $0.2\,T$, and the first image is one time step after the membrane burst. This translates to 0.10, 0.14, 0.14, and 0.18 s for the four aspect ratios shown. The last image shows the flow field just as the buoyant fluid
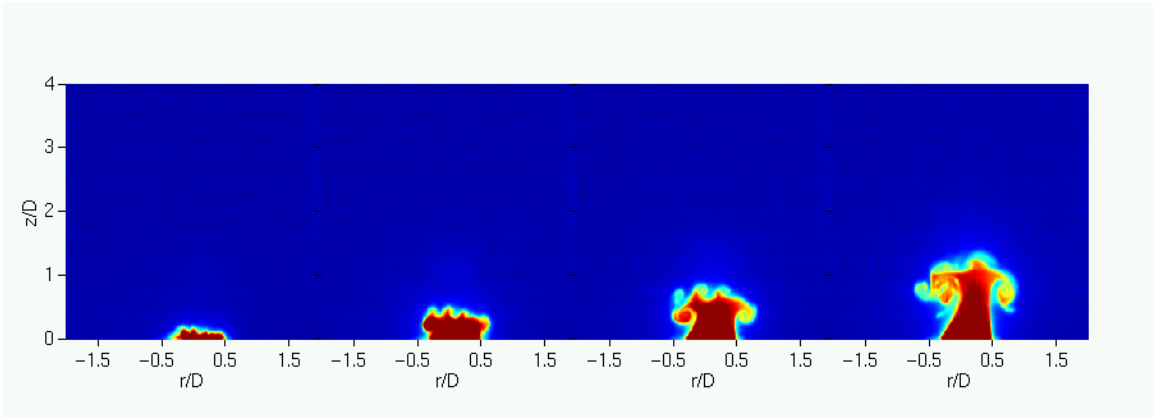
Figure 4.1: PLIF images for an aspect ratio of 2.

has been completely discharged from the tube. However, a thin boundary layer containing some buoyant fluid remained in the tube for most of the duration of the experiments.

The development of the lowest aspect ratio of L/D = 2 has been discussed in Chapter 3. A series of images for this aspect ratio, Fig. 4.1, is included for reference. The most notable features of the flow field at this point is the significant development of the Rayleigh-Taylor instability at the fluid interface.

Figure 4.2 shows the development of the flow field for an aspect ratio of L/D = 4. The development of the Rayleigh-Taylor instability is evident in the first two PLIF images, and the remnants of the structures formed remain during the fluid discharge phase. The roll up process is very similar to the previous case. The roll up is somewhat more developed than in the previous case, as can be seen in the second image. However, by the third frame, the roll up process has been severely distorted. This is evident in the lack of distinct bands of ambient and buoyant fluid within the core region. Much of this internal structure has disappeared. By the final frame, only the remnants of the initial roll up process are visible as bright cores of buoyant fluid. The disruption of the initial roll up appears to have been caused at least partially by the radial propagation of the structures formed by the Rayleigh-Taylor instability along the leading edge of the flow. Although the roll up process is still severely disturbed in this case, it more completely developed than for the previous case.
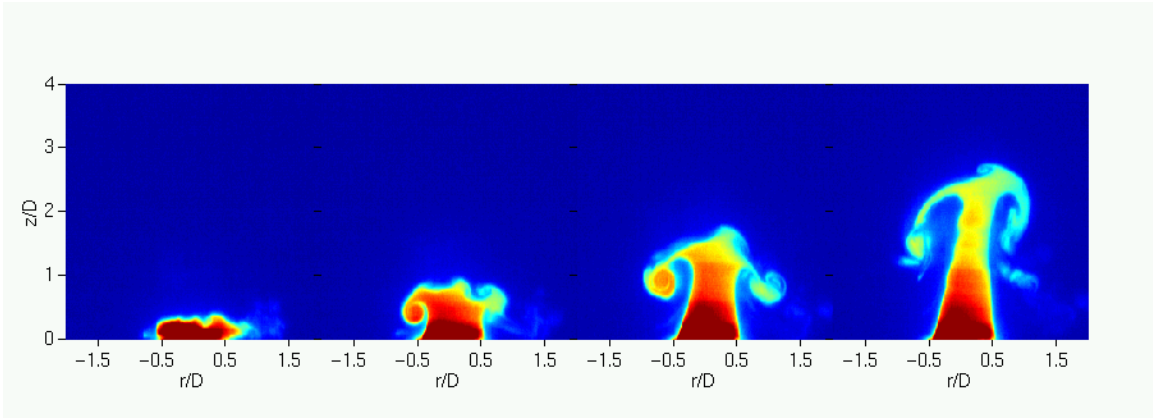
43

Figure 4.2: PLIF images for an aspect ratio of 4.

A series of PLIF images for an aspect ratio of L/D = 6 is shown in Fig. 4.3. The development of the Rayleigh-Taylor instability is still visible, however, the number of disturbances on the leading edge has been reduced. In the second frame, the beginning roll up of the boundary layer can be clearly seen on the left hand side of the flow, while on the right hand side, the development has been inhibited by the initial disturbance. The next image shows that there is another factor contributing to the breakdown of the initial roll up. The core region on the left side has not yet been visibly affected by the disturbances formed due to the Rayleigh-Taylor instability, yet the internal structure has begun to degrade. The longer acceleration period associated with the large aspect ratio has allowed the flow to develop more completely before the instability at the interface affects the roll up process. However, the breakdown of the core region means that some other mechanism is also acting to disturb the boundary layer roll up. By the final frame, the leading edge disturbances have had enough time to propagate to the core region, and on the left side, this has resulted in the initial core being separated from the leading edge and falling behind. A secondary roll up is visible at this point. Although the roll up is still disturbed under the action of both the instability and buoyancy within the core, the core development is even more pronounced than the previous cases. This indicates that the greater momentum generated for larger aspect ratios allows a the boundary layer roll up to have a greater effect
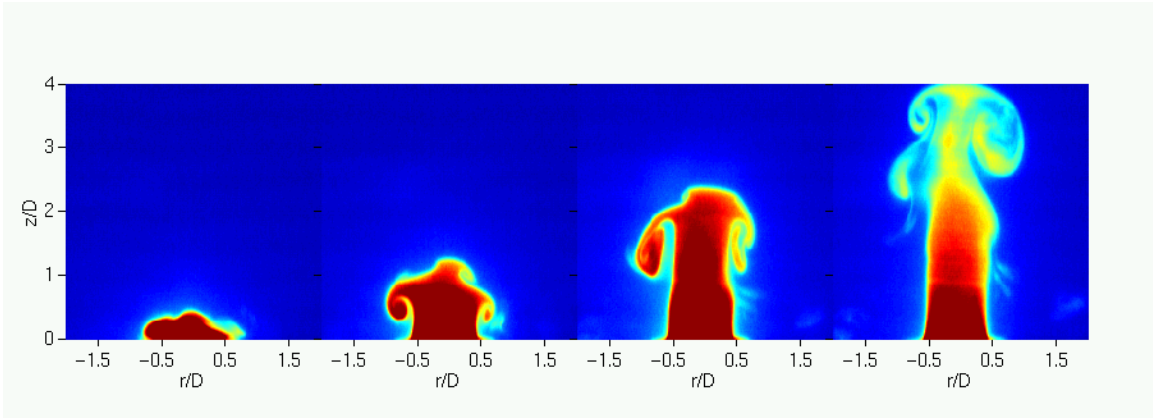
Figure 4.3: PLIF images for an aspect ratio of 6.

on the flow development.

PLIF images of the starting phase are shown in Fig. 4.4 for an aspect ratio of L/D = 8. Even here, the initial two frames show the presence of the Rayleigh-Taylor instability. Also, in the second frame the right hand side roll up appears to have not started. However, by the third image, the effect of the greater momentum in this case is clear. The initial disturbances that were formed at the leading edge are no longer visible, and the internal structure of the left hand side is still visible. The right hand side also shows the development of a core region. The action of the buoyant forces is still evident in the distortion of the core regions. The results of these somewhat opposing forces is more clearly seen in the final frame. At this point, the overall structure is similar to that of a purely momentum driven flow. The core region belies this fact however. Both sides of the flow show that most of the roll up structure within the core regions has been destroyed. The lack of any visible signs of the initial leading edge instability is notable as well.

From this series of figures, it is apparent that the presence of buoyancy significantly impacts the initial flow development. For smaller aspect ratios, and correspondingly smaller contributions of momentum, the fluid interface instability has sufficient time to develop and subsequently disturb the vortex ring formation process. As the aspect ratio increases, the interface instability plays a smaller and smaller role, while the boundary layer roll up
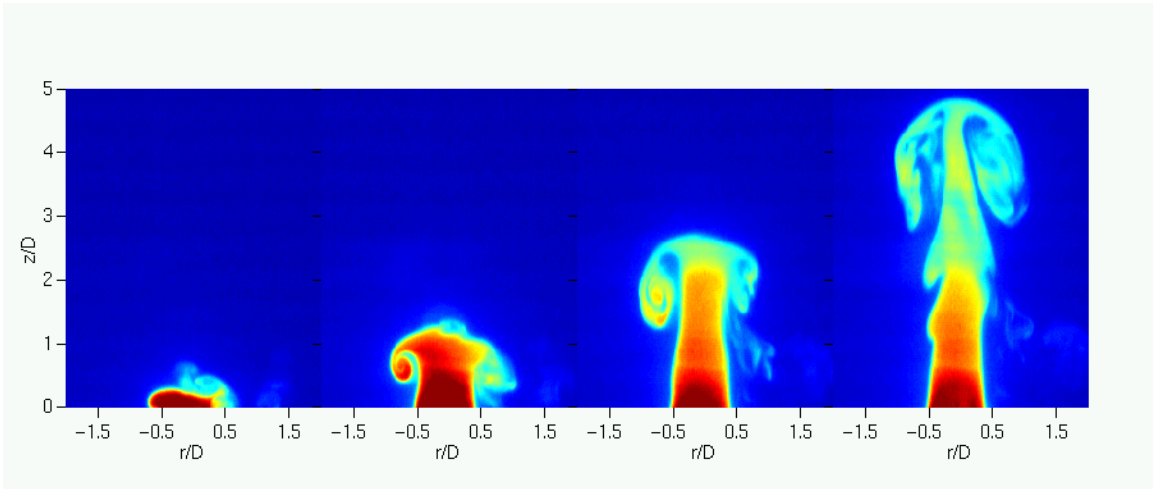
Figure 4.4: PLIF Images for an aspect ratio of 8.

is more complete. There is also another aspect of the flow development. The presence of buoyancy affects the vortex ring development beyond simply amplifying any disturbances created during the fluid release. Even for the largest aspect ratio examined, the distinct bands of ambient and released fluid usually associated with a boundary layer roll up was no longer visible by the time the fluid had been completely discharged.

A short time after the fluid had been discharged from the tube, the fluid would begin to slow, and the flow structure would undergo significant changes. At the point where the fluid has been completely discharged, there is still a significant amount of unmixed buoyant fluid for the larger aspect ratios. The phase following the fluid released can be characterized by large changes in the buoyant fluid concentration and distribution. Figures 4.5 to 4.8 show a series of images for each aspect ratio. Each series starts one time step after the fluid has been discharged and continues in equally space increments until the flow field begins to leave the region that was imaged (0 to 12 D. The resulting time steps for each of the four aspect ratios are 0.55, 0.25, 0.20, and 0.17 s. Each of the images has been assigned false color, and the color scaling has been changed to make the flow structure visible. For many of the later frames the fluorescence intensity of the image was very low. The development of the smallest aspect ratio, $L/D = 2$, has already been discussed, but an image is included

for comparison. Most notably, the buoyant fluid quickly becomes mixed with the ambient fluid, and rapidly develops into a widening vortical ring structure.

Figure 4.6 shows a series of PLIF images for an aspect ratio of $L/D = 4$. The behavior of this flow is very different from that of the previous case. In the first frame, undiluted or weakly diluted buoyant fluid is still visible in the central column region as well as near the leading edge. There is also some indication of the vortex ring type structure, with two lobes on either side of the central column like region. This situation changes by the second frame. Here, the flow has developed into an asymmetrical "blob" of buoyant fluid, with the highest concentrations in the interior. One interesting feature of this particular experiment is the trailing core of fluid on the left. This is a remnant of the initial roll up of the boundary layer which has been left behind. This was formed due to the interference of the Rayleigh-Taylor instability during the discharge process, and may account for the large asymmetry seen. The third and fourth images show that the buoyant fluid is indeed remaining a coherent mass, while it expands and becomes more diluted. The bright core region appears to be moving with approximately the same celerity as the rest of the flow.

The development of the flow field for an aspect ratio of $L/D = 6$ can be seen in Fig. 4.7. At the initial frame, the flow still contains a significant quantity of unmixed buoyant fluid. Also, the flow consists of a column of relatively constant width, topped by a ring like structure. In the second image, the fluid has diluted considerably over much of the region. The central column of fluid has been almost completely incorporated into the buoyant mass leading the flow. There are some remnants of the boundary layer visible as small vortex cores trailing the major features of the flow field. At this point, the interior flow still contains relatively sharp gradients in concentration, indicating that there may be areas where the buoyant fluid is not highly mixed. However, by the third frame, the flow is becoming much more uniform, similar to the $L/D = 4$ case. Some remnants of the vortical ring structure are still visible at this point, as the higher concentrations of buoyant fluid are located near the core regions. In the final frame, it is clear that the fluid mass is now moving as a

single unit, while there is still some indication of the original roll up process.

The development of the largest aspect ratio, $L/D = 8$, shown in Fig. 4.8, is similar to the $L/D = 6$ case. In the first image, the flow consists of large concentration gradients, with regions of buoyant and ambient fluid in close proximity. There are clearly two regions within the flow, a central column, capped by a leading vortical structure. There are also several distinct "cores" visible in the leading structure. This structure persists to the next image, however, the internal structure of the flow has begun to change. The distinct "cores" have all but disappeared. Following the flow to the next image, mixing between the buoyant and ambient fluids has begun in earnest. The leading region has become a ball like cap. In the last two images, the transformation of the flow towards a coherent mass can be clearly seen. In the third frame, there are two regions of more concentrated buoyant fluid, with a small gap between them. However, by the final image, this gap has nearly disappeared, as the trailing mass is being engulfed by the leading mass from the rear. This engulfment can be seen as a consequence of the slowing of the leading portion of the flow as it is diluted more rapidly than the trailing portion.
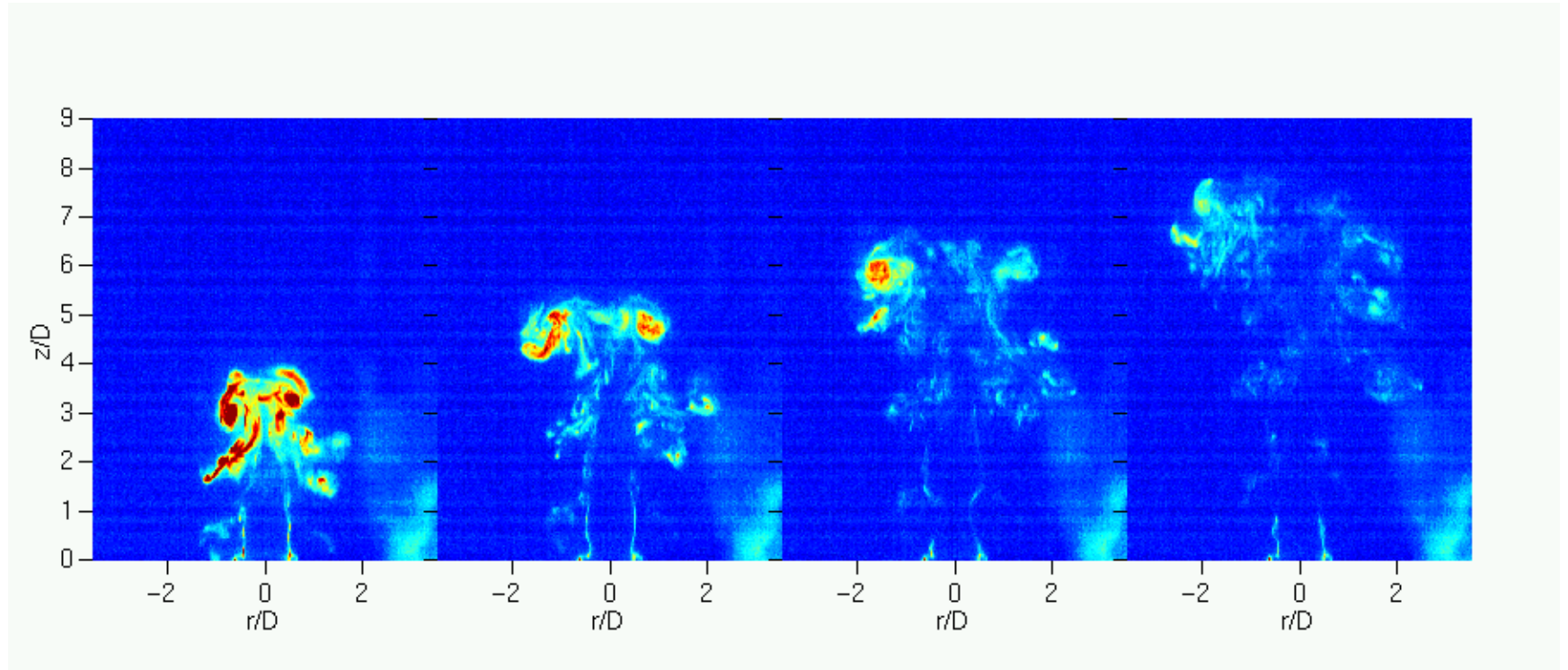
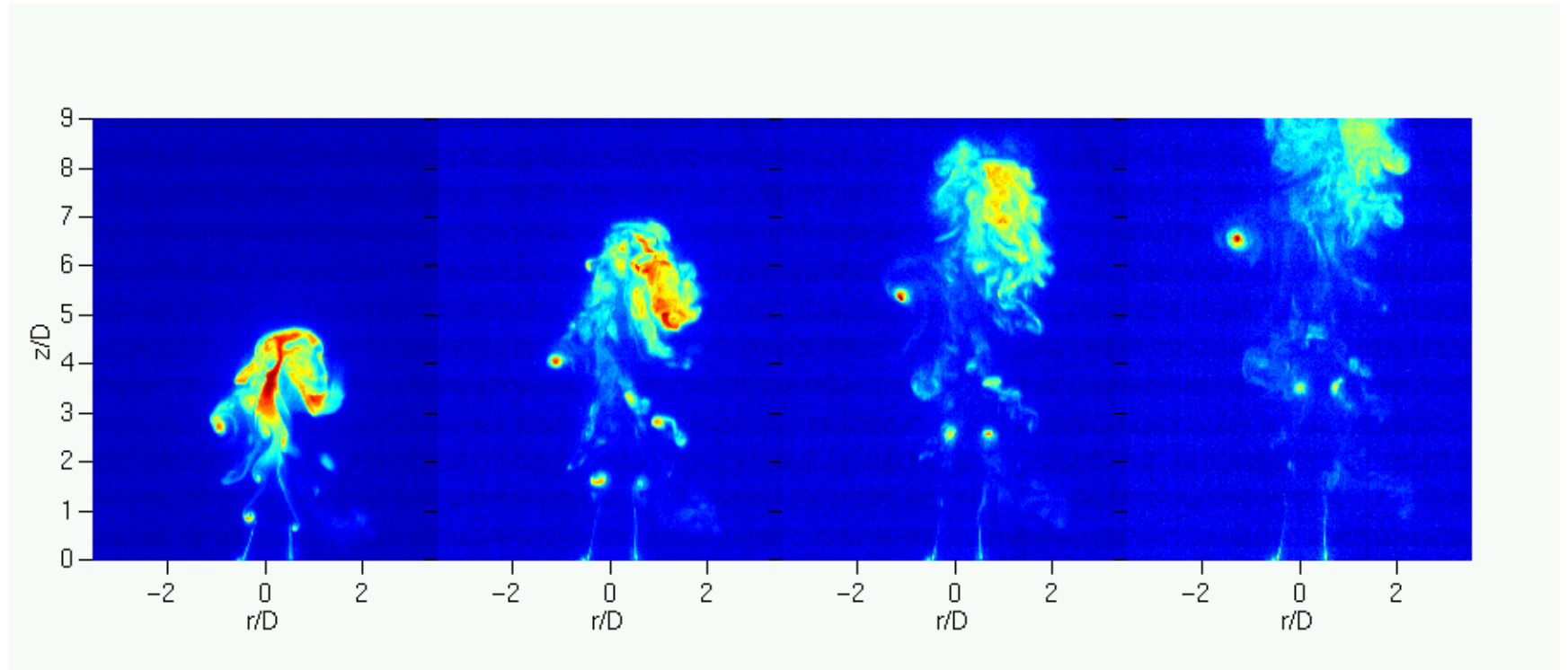Figure 4.5: PLIF images for an aspect ratio of 2 after discharge.

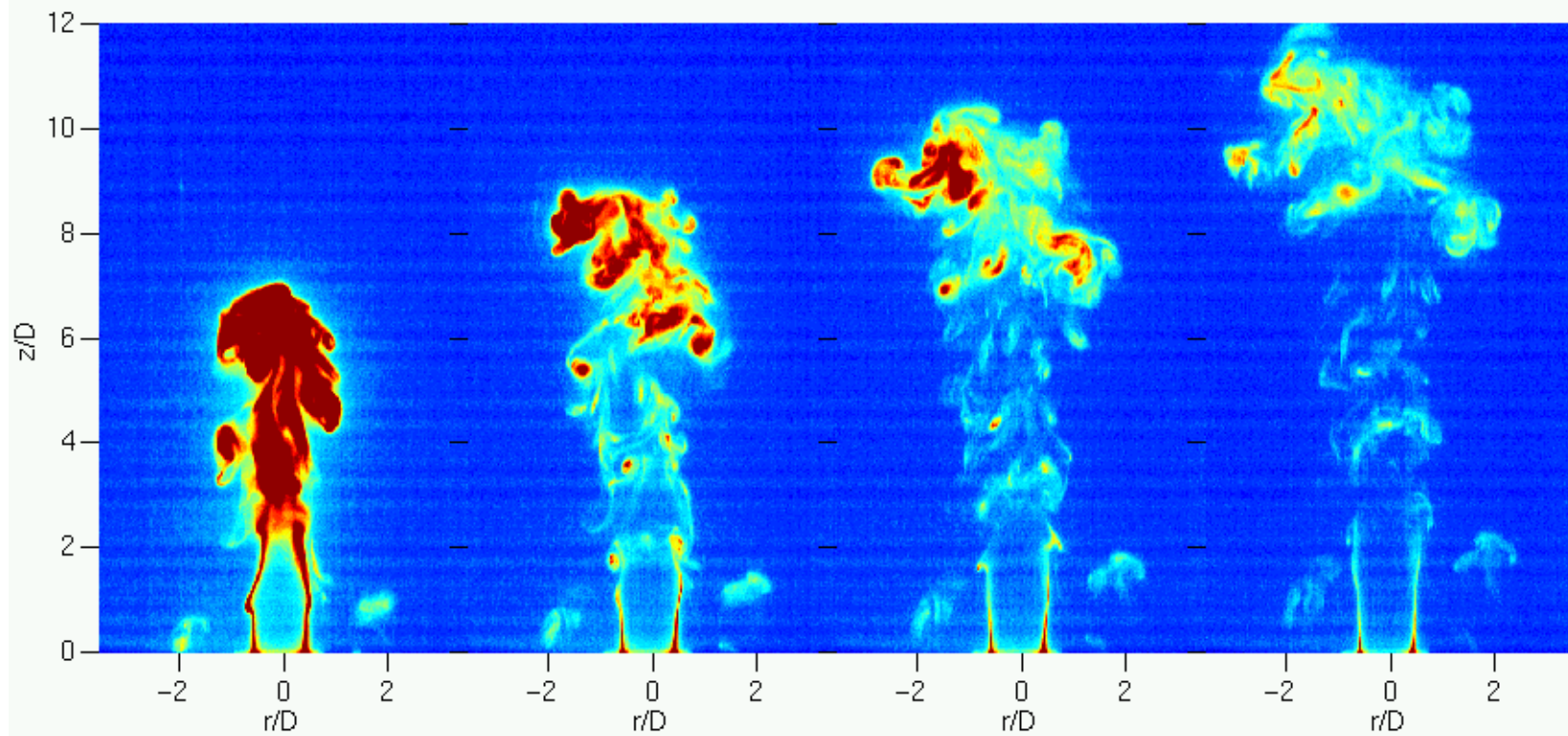Figure 4.6: PLIF images for an aspect ratio of 4 after discharge.

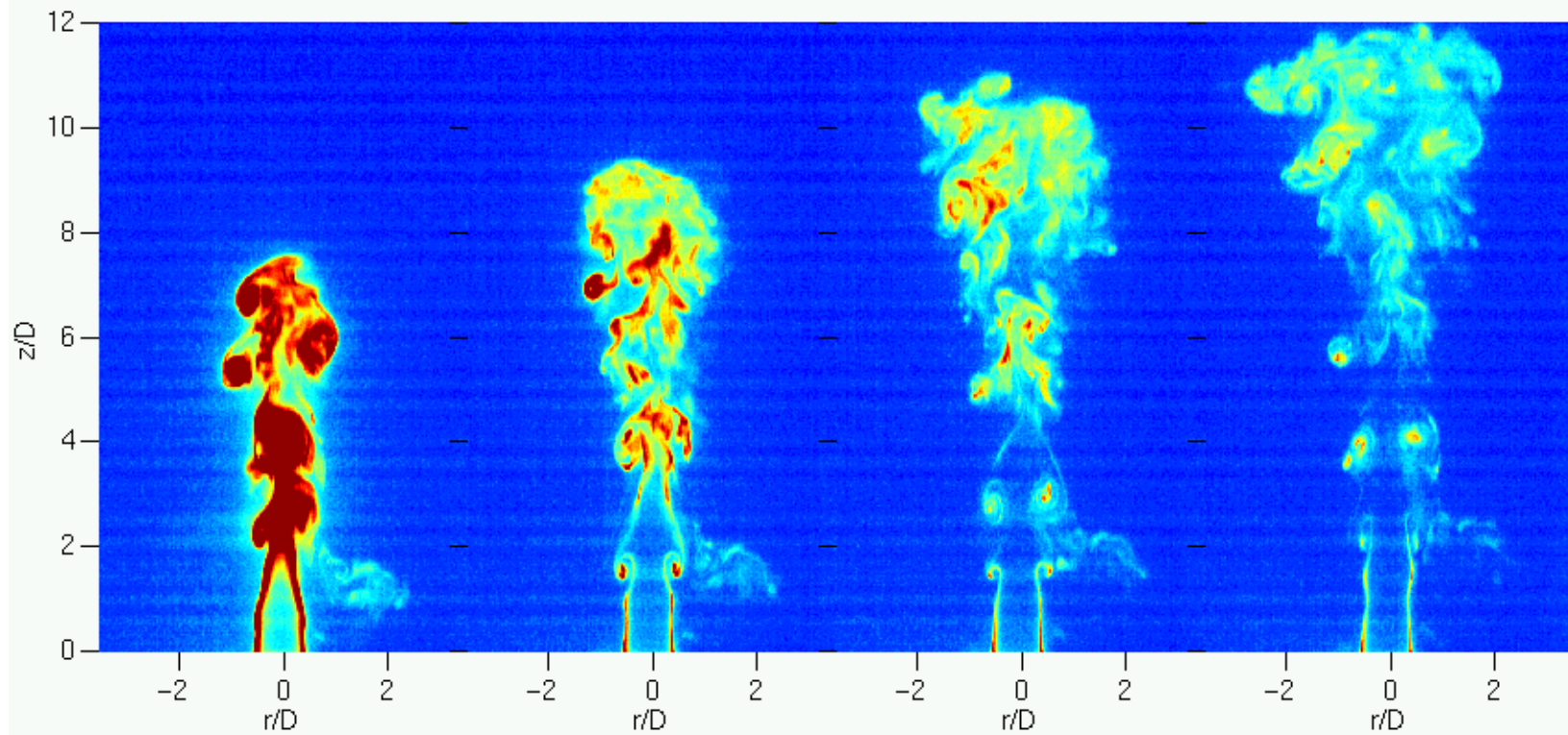Figure 4.7: PLIF images for an aspect ratio of 6 after discharge.

Figure 4.8: PLIF images for an aspect ratio of 8 after discharge.

The fact that the presence of buoyancy, and therefore baroclinic torques, is responsible for the disruption of the conventional boundary layer roll up is also supported by a set of experiments investigating the effect of shock waves on compressible vortex rings carried out by Cetegen & Hermanson[17]. The shock waves create regions were large pressure and density gradients exist, not necessarily parallel to the existing flow field. The resulting images after the shock passage look markedly similar to the images of the current buoyant flows.

4.2 Flow Field

In order to better understand this flow field, the DPIV technique was utilized. First the vorticity fields were examined and compared to the PLIF images obtained. However, it is necessary to keep in mind the wide gap in resolution of these two techniques when comparing the results. Also, several integral measures of the flow development were examined. These were the circulation, impulse, and energy.

Figure 4.9 shows the vorticity fields for each of the aspect ratios at the time when the fluid has been completely discharged from the tube. The vorticity contours were placed at intervals of 10% of the peak vorticity, and all contours below $0.5s^{-1}$ were ignored. The most notable difference between these vorticity fields and the PLIF images seen above is the lack of very small scale features. However, this must not be interpreted as a lack of fine scales, it is due to the resolution difference of the two techniques. The large scale structures identified by this technique are examined next.
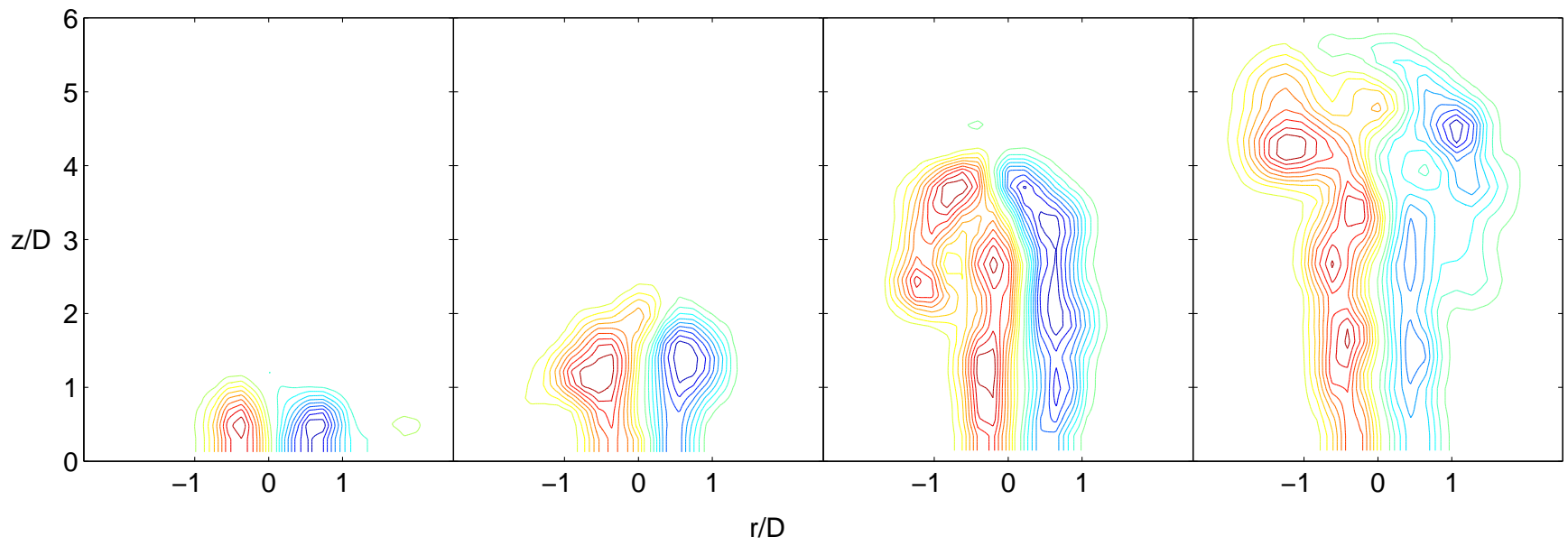
Figure 4.9: Vorticity field at the time, t=T, when the fluid has been discharged, for each aspect ratio.

For the aspect ratio of $L/D = 2$ (the leftmost frame), the flow has not even formed into a vortex ring. This occurs one or two DPIV frames (33 - 66 ms) later. This aspect ratio was discussed in detail in Chapter 3. The next vorticity field shows a snapshot of the flow for the aspect ratio of $L/D = 4$. Here, the contours remain attached to the generating tube, however, the roll up is evident at the front of the flow and the attached contours are relatively weak. At an aspect ratio of $L/D = 6$, several changes are evident. The contour at 30% of the peak vorticity contains all of the higher vorticity regions, however there are multiple cells evident at the higher vorticity levels, similar to what was seen in the PLIF images. This indicates that the large scale (on the order of the flow width) structures are affected by action of the baroclinic torques. At an aspect ratio of $L/D = 8$, this trend is even more evident. The flow consists of a column like region of vorticity capped by region of high vorticity. The cellular structure is visible here as well. Again, the higher vorticity levels are all bounded by the 30% contour. The flow structure in these early stages shows a change between the aspect ratios of $L/D = 4$ and 6. For the lower aspect ratios (2 and 4), the buoyant fluid was all incorporated into a single large scale vortical structure. However, for the larger aspect ratios (6 and 8), the flow initially formed a cap/column structure. This then developed into a single larger vortical structure. This behavior was consistent in all of the experiments.

Figures 4.10 to 4.13 show the vorticity fields for each of the aspect ratios from the time the tube had discharged all the buoyant fluid to the time the flow left the recorded region ($z/D < 7$). Each of the sequences consists of six vorticity fields equally spaced in time, translating to Δt's of 0.20, 0.10, 0.05, and 0.02 s. The aspect ratio of $L/D = 2$ flow was discussed in Chapter 3.

Figure 4.11 shows a series of images for the aspect ratio of $L/D = 4$. The initial frames show the vortical ring structure developed as the tube discharged. However in the second through fifth frames, the multi-cell structure seen at higher aspect ratios earlier begins to be evident. This cellular structure appears to be accompanied by an actual separation of small

masses of fluid in and around the central region of the flow.

Figure 4.12 shows a similar series of snapshots for an aspect ratio of $L/D = 6$. In this case, the leading vortical structure already contains several distinct cells. In the first four frames, this cellular structure continues to develop, but it is notable that the trailing flow appears to remain attached. The last two frames show the beginning of radial expansion. This is accompanied by the generation of intermingled regions of both signs of vorticity within the central core of the flow field.

Although the development that was recorded for an aspect ratio of $L/D = 8$ was limited to only a brief period after the flow had been discharged from the tube, Fig. 4.13 is included for completeness. It confirms many of the observations of the smaller aspect ratios as well. Notably, the column/lump structure is preserved in most of the frames. However, in the later frames, it is difficult to determine where the buoyant fluid ends and the trailing flow begins. Also, the radial expansion of the flow accompanied by the development of central sub peaks of vorticity can be seen.
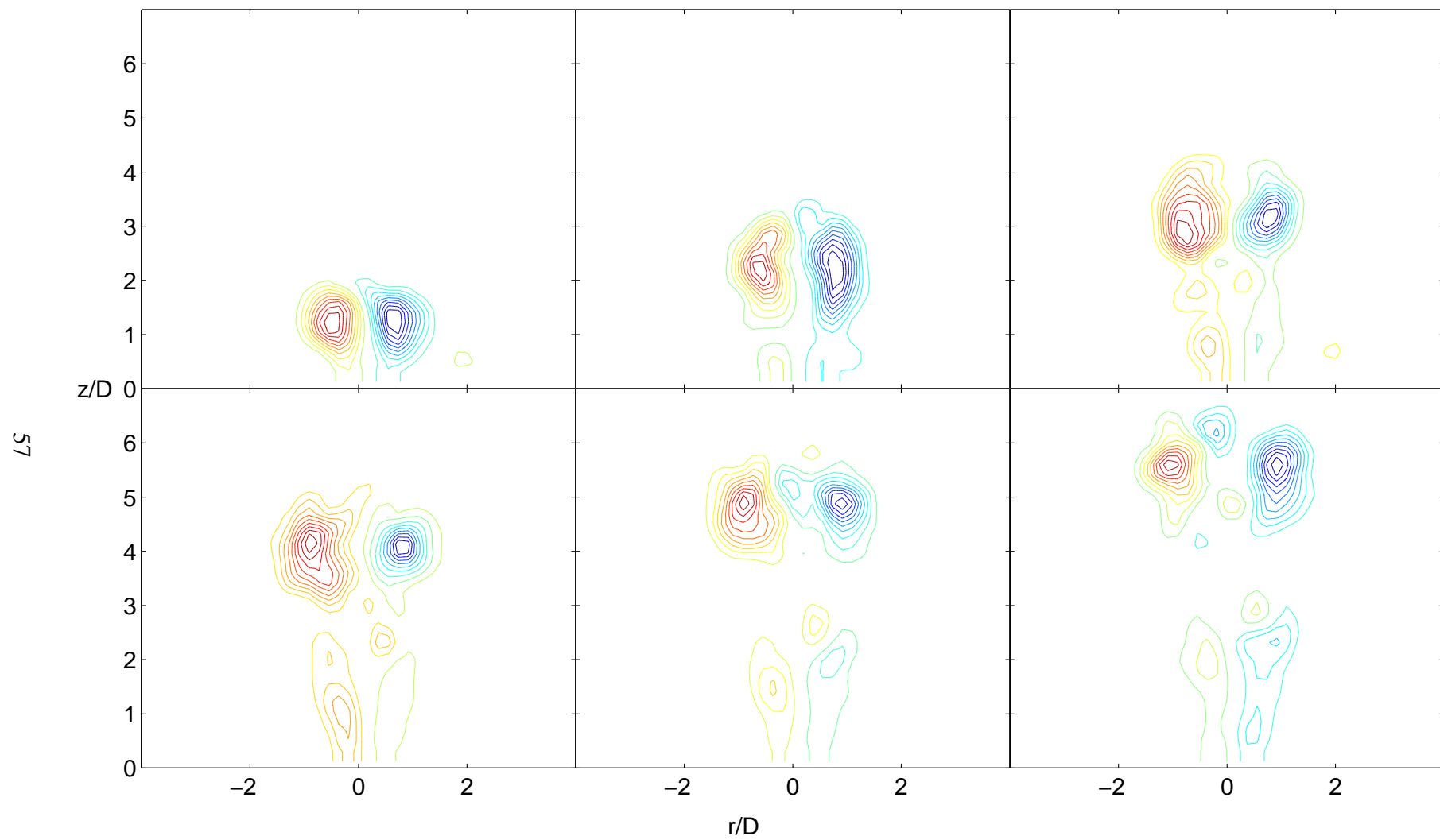
Figure 4.10: Vorticity field evolution from completion of discharge to the last usable frame for $L/D = 2$. $\Delta t = 0.12s$
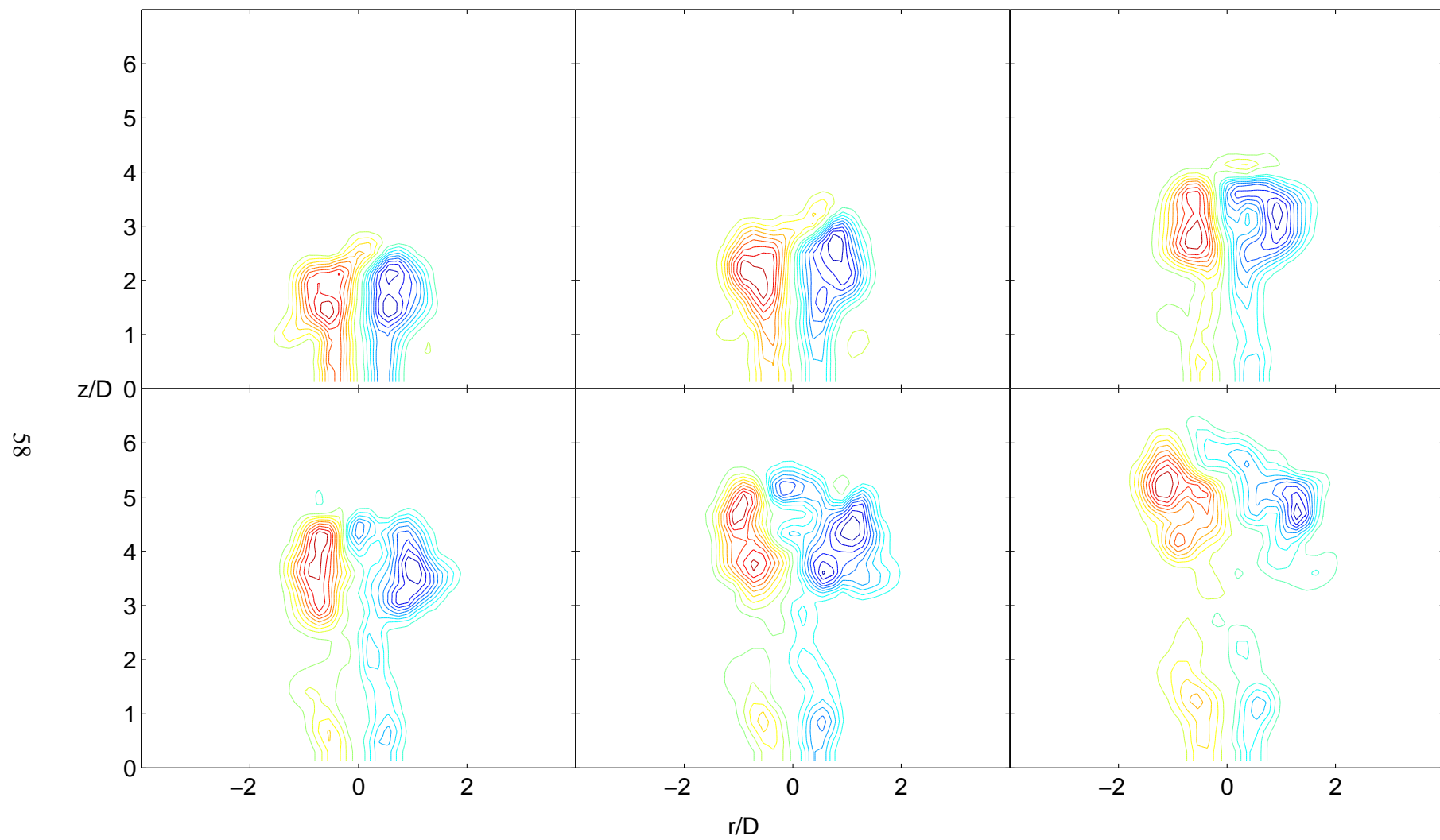
Figure 4.11: Vorticity field evolution from completion of discharge to the last usable frame for $L/D = 4$. $\Delta t = 0.05s$
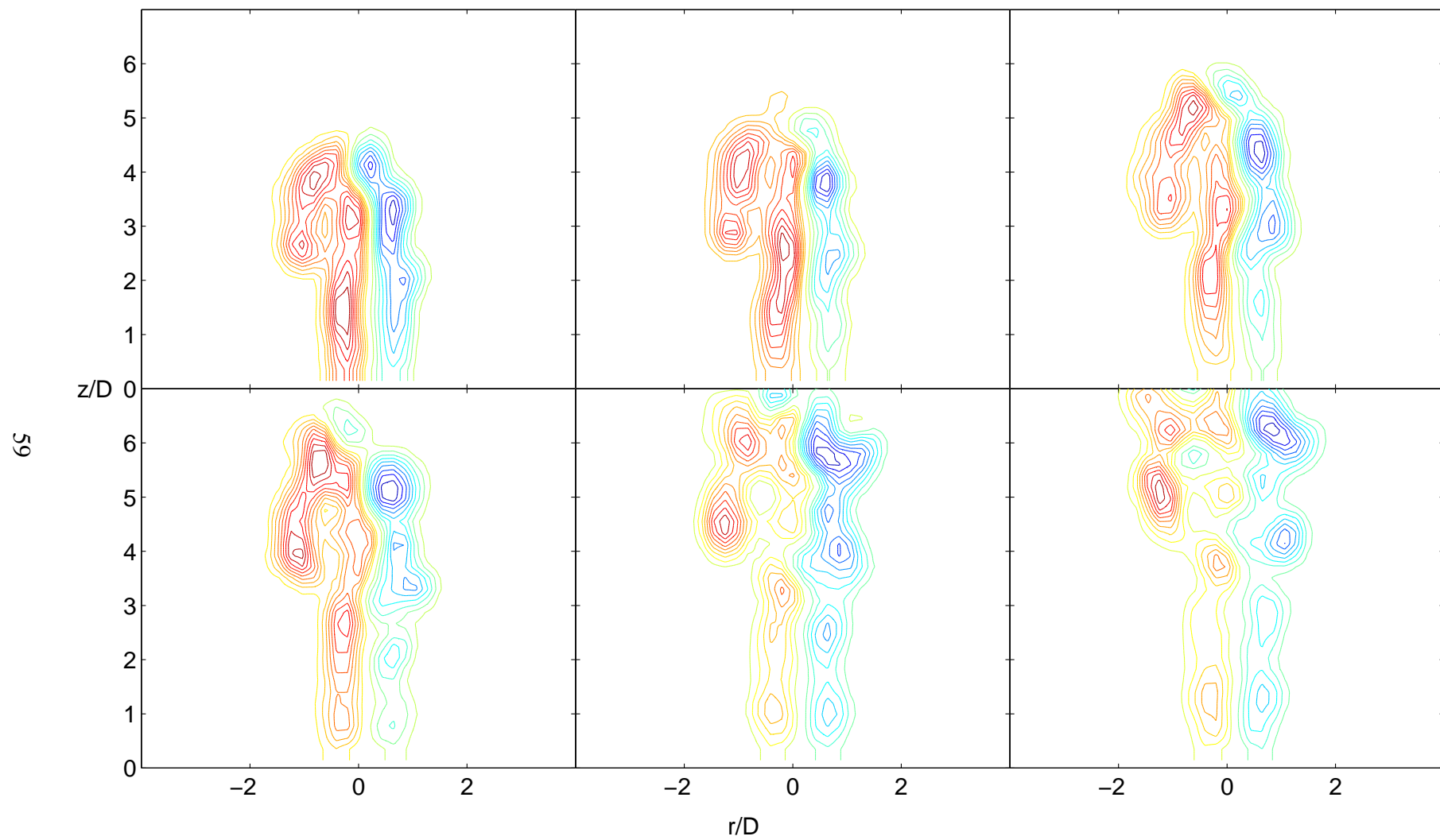
Figure 4.12: Vorticity field evolution from completion of discharge to the last usable frame for $L/D = 6$. $\Delta t = 0.03s$
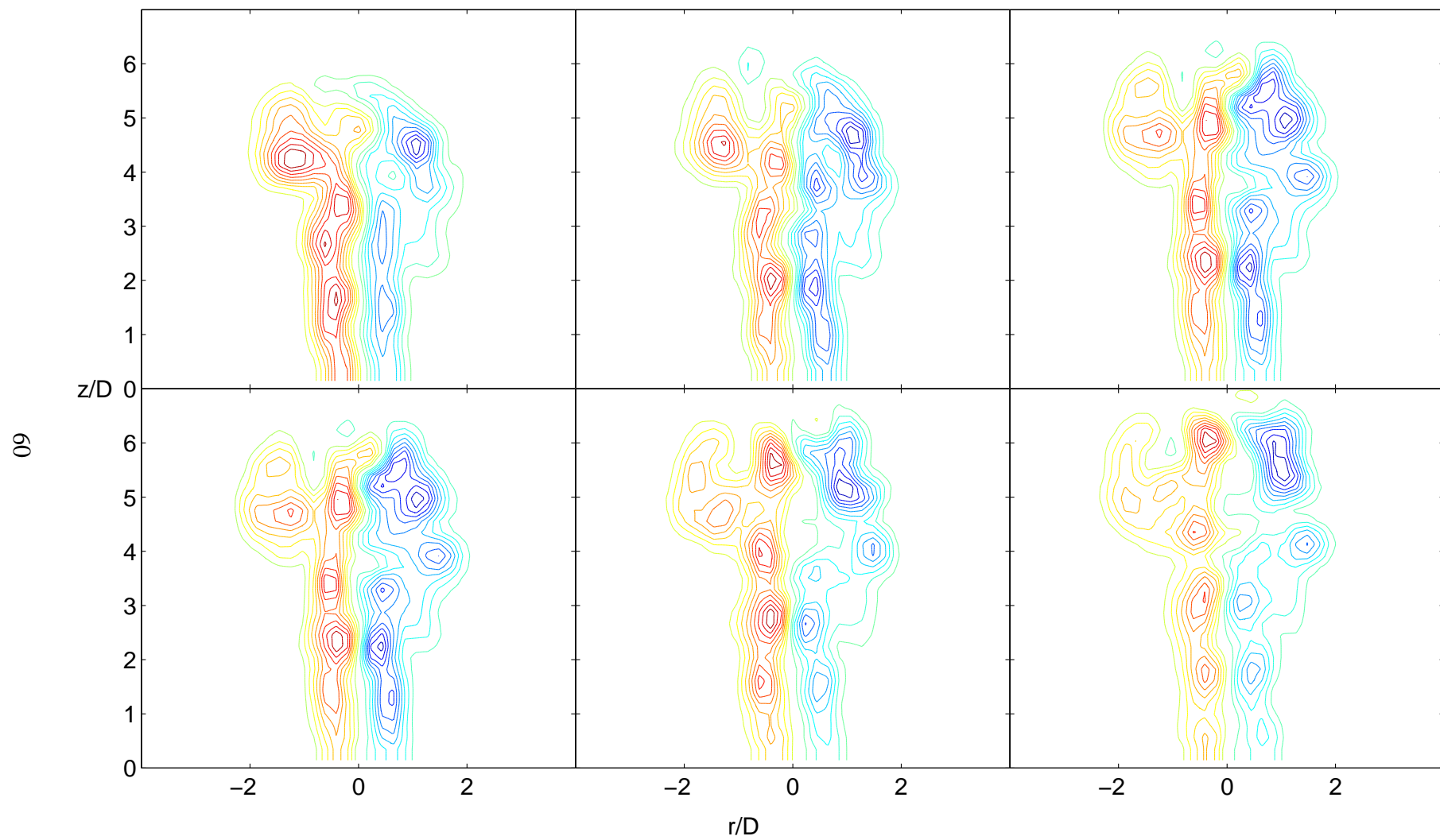
Figure 4.13: Vorticity field evolution from completion of discharge to the last usable frame for $L/D = 8$. $\Delta t = 0.02s$

The lack of a clear separation of the leading vortical region of the flow for the two highest aspect ratios is important. In similar experiments with momentum driven starting flows, the initial vortical roll-up develops into a separate vortex ring that propagates at a higher celerity than the trailing flow. The buoyant case appears to operate in the opposite manner. The initial roll up of the boundary layer forms into a vortical lump at the head of the flow. For aspect ratios of $L/D > 4$, the leading vortical structure is initially followed by a column of buoyant fluid. However, this column does not separate from the leading flow, but is reincorporated during the transition to a thermal like flow. This initial stages of this behavior can be seen in the last DPIV frames shown above as well as the later PLIF images.

An aspect difficult to present in individual vorticity fields is the dynamics of the motion of the cellular vorticity structure. As expected, the entire vortical region appeared to slowly rotate in the same direction as the local vorticity. The cells of vorticity appeared to be created predominately in the central region. Those formed near the leading edge were usually swept around the perimeter of the flow. It also appeared that cells of opposite sign would occasionally disappear in pairs, indicating annihilation of the two opposite signs of vorticity. This phenomenon was most prevalent after the fluid had been completely discharged.

4.3 Transition

It will be shown that the development of the buoyant flows could be divided into two phases, an initial acceleration period followed by a thermal like phase. These two phases were divided by a transition period where the flow began to decelerate and the flow structure changed dramatically.

The clearest method of divided the two flow regimes was obtained by measuring the position of the leading edge of the flow as a function of time from the PLIF images. The
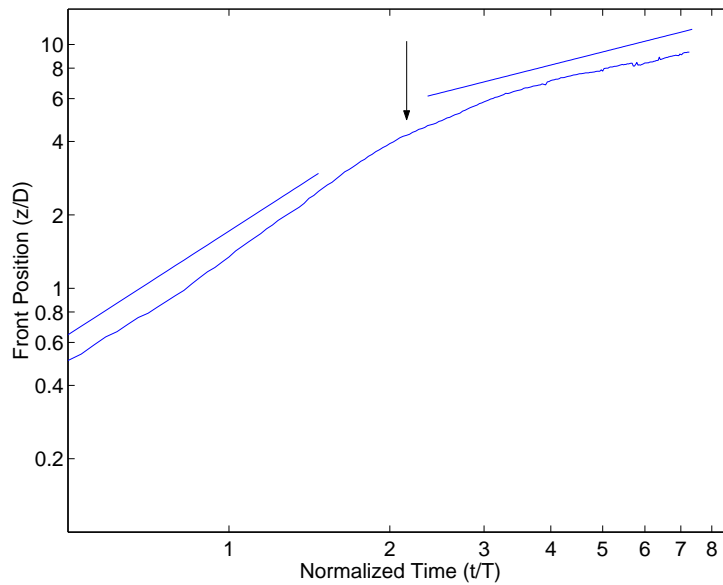
Figure 4.14: Leading edge position (z/D) for an aspect ratio of 2. The two lines show the slope of the curve during the two phases of the flow. The arrow indicates the transition point.

leading edge was taken to be the most downstream parcel of fluid that had a concentration value above a specified threshold. The threshold value used was chosen to eliminate the background from the image. For most of the images obtained, the background fluorescence level with the laser on was 16 out of 255.

Figure 4.14 shows the progression of the leading edge of the flow for an aspect ratio of 2 in a log-log plot. Two regions with nearly constant slope are indicated. The initial region corresponds the flow acceleration. The final region corresponds to a thermal-like deceleration. A transition point was defined where the thermal-like phase began. In order to quantify the transition point, a power law was fitted to the thermal-like region of the progression data. The transition point was taken as the point where the data approached this curve to within 10%. This point is marked in Fig. 4.14.

Although the development described above was the clearest for the aspect ratio of 2, the larger aspect ratios showed similar development. Figures 4.15 to 4.17 show the leading edge development for the aspect ratios of 4, 6, and 8. For these larger aspect ratios, the
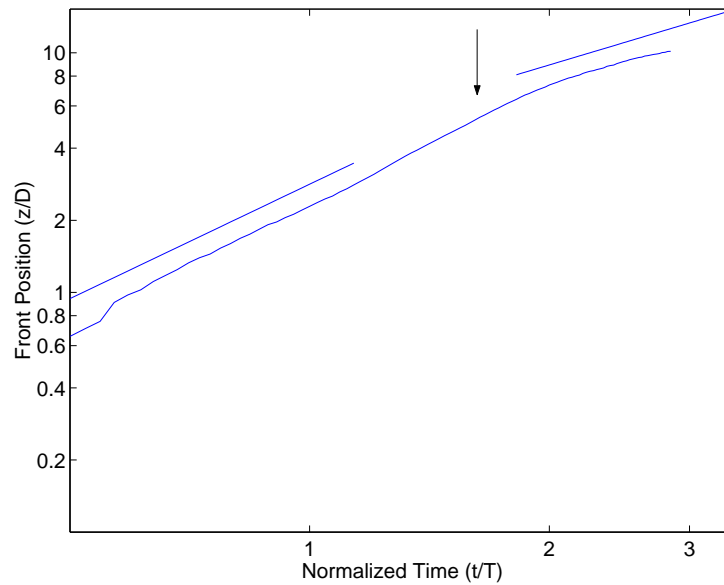
Figure 4.15: Leading edge position (z/D) for an aspect ratio of 4. The two lines show the slope of the curve during the two phases of the flow. The arrow indicates the transition point.

final thermal-like state is less pronounced since the transition does not occur until further downstream.

Figure 4.18 shows PLIF images of the flow at the transition point for several aspect ratios. The flow at the transition point had a broad range of concentration values. This was consistent in most of the experiments carried out.

Figure 4.19 shows the transition distance plotted against the cube root of the initial volume, with both values normalized by the tube diameter. A dimensional analysis based on the tube diameter (D), initial released volume (V_o), and the transition distance (z_{tr}) results in this form. There is some indication that there may be a dependence on the tube diameter, however, there is not enough data to be certain.

Figure 4.20 is an image of the thermal like state for the tube with an aspect ratio of 2, about 8 diameters downstream. Here, the mixing has greatly reduced the concentration, so that the structure is difficult to visualize. There is less complexity in the flow structure. This type of structure was seen mainly for this aspect ratio. The flows generated by the
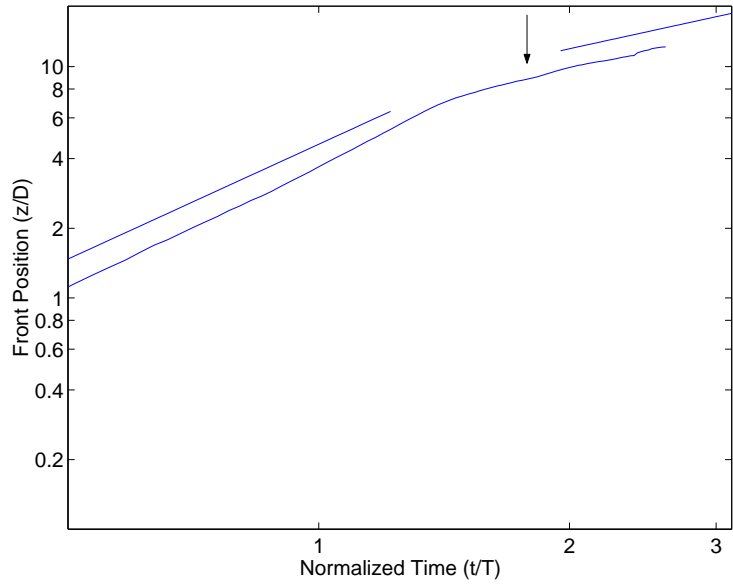
63

Figure 4.16: Leading edge position (z/D) for an aspect ratio of 6. The two lines show the slope of the curve during the two phases of the flow. The arrow indicates the transition point.
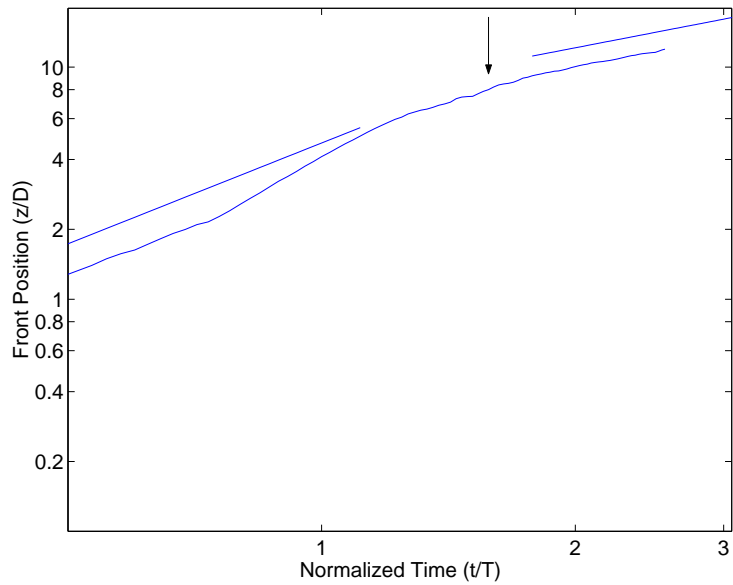

Figure 4.17: Leading edge position (z/D) for an aspect ratio of 8. The two lines show the slope of the curve during the two phases of the flow. The arrow indicates the transition point.
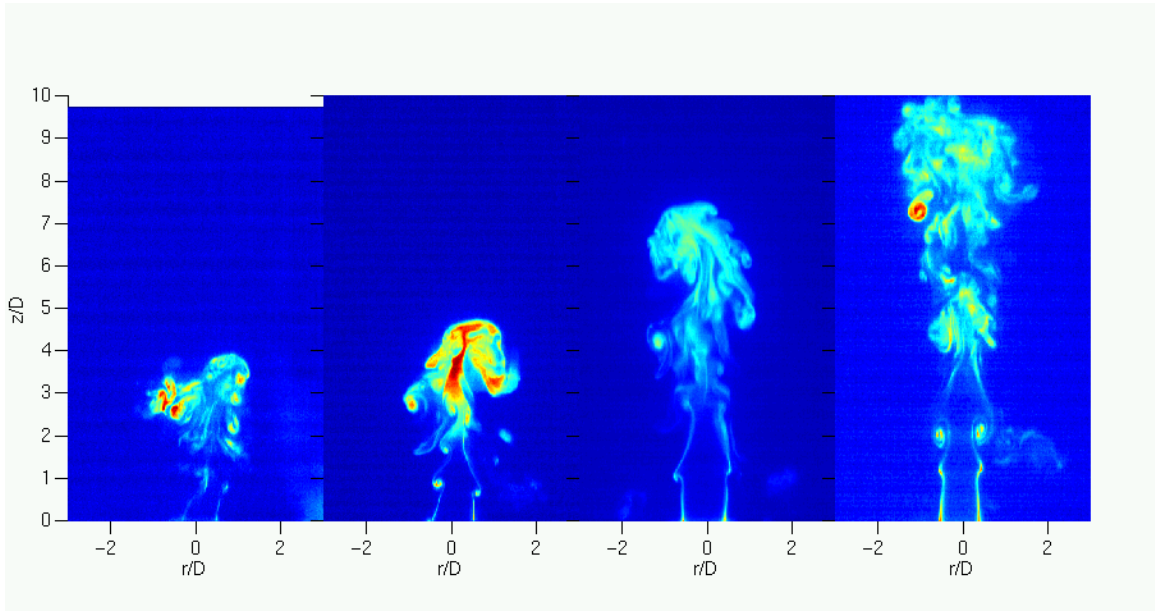
Figure 4.18: PLIF images of the flow structure at the transition point for aspect ratios of 2, 4, 6, and 8.
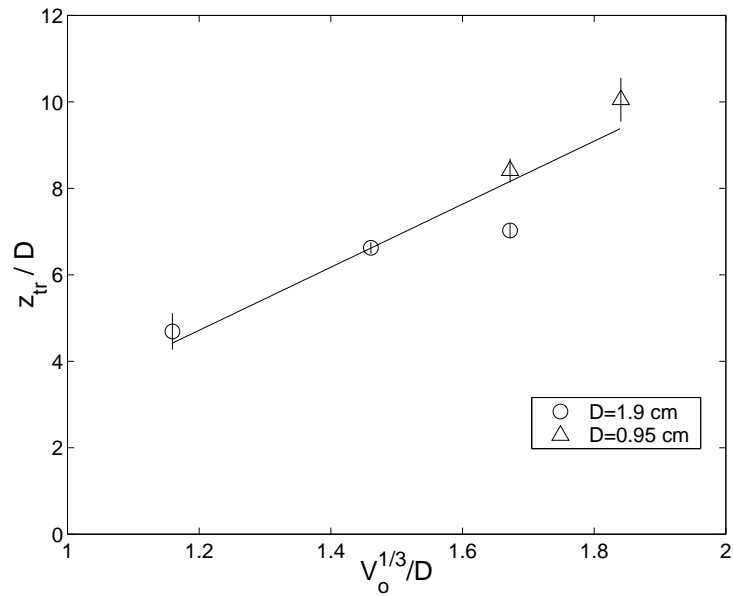

Figure 4.19: Leading edge position at the transition point.
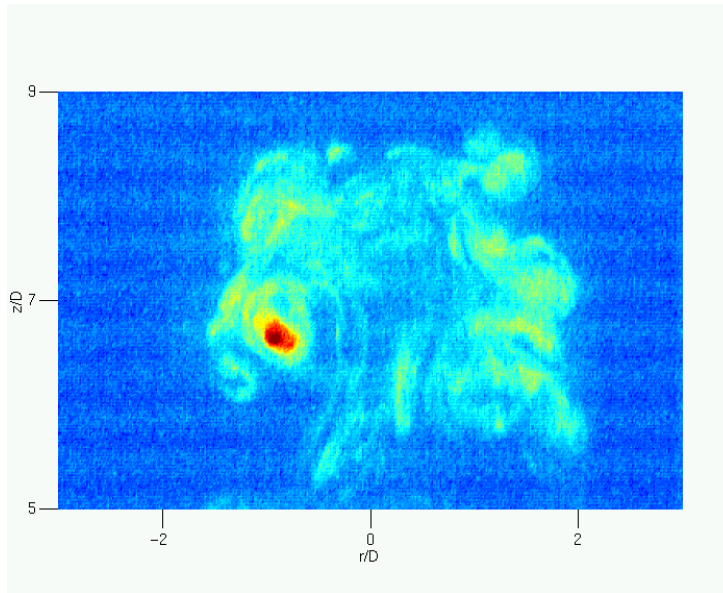
Figure 4.20: PLIF image of a thermal-like state for an aspect ratio of 2.

larger aspect ratio tubes did not appear to reach a thermal-like structure within the first 7 diameters.

However, there is some indication that the flow for all the aspect ratios was approaching the thermal state. In the far field, the leading edge position of a thermal is proportional to the square root of time. The average of the exponent for the power law fit to the deceleration phase for each aspect ratio ranged from 0.6 to 0.7. This is not too far from the expected value of one half.

4.4 Integral Measures

The DPIV data were also used to compute the development of the circulation, impulse, and energy for all four aspect ratios. These values were computed inside an iso-vorticity contour at $1\ s^{-1}$.

4.4.1 Circulation

The circulation was computed using the previously described method of the line integral. These results were then examined to determine the effect of the initial geometry on the final circulation value. Figure 4.21 shows the development of the circulation for an aspect ratio of $L/D = 2$, as discussed in the previous chapter. Figure 4.22 shows the development of the circulation for both the clockwise and counterclockwise vortices for an aspect ratio of 4. The circulation values for the two sides match each other very closely, indicating that the behavior seen is not due to movement of the vorticity into or out of the measured plane.

The initial phase of the flow is dominated by a rapid increase in the circulation. This increase continues after the tube is empty. A sharp transition region follows the increase. This transition region is sometimes marked by a decrease in the total circulation. The final phase is marked by a relatively constant total circulation in the flow. Similar figures for aspect ratios of $L/D = 6$, and 8 are included in Figs. 4.23 and 4.24. It should be noted that these two tubes had a smaller diameter, so the absolute values of circulation are lower than the aspect ratios of 2 and 4. The shape of all of the curves is very similar. The most notable difference is the extent of continued increase in circulation after the fluid has been discharged. Since the tube boundary layer is no longer contributing to the flow, this increase must come about due to the action of the buoyant forces on the fluid. Also, the good agreement between the value obtained for each sign of circulation indicates that the increase is likely not due to any kind of marked asymmetry developing. The final leveling off is more difficult to determine for the larger aspect ratios, as they do not reach this state until they are nearly out of the imaged area.

Comparing the transition points in Figs. 4.14 to 4.17 with the start of the constant circulation region shows that these two events occur near the same time. The ambiguity of the transition point and the starting point for the constant circulation region makes it difficult to determine a mathematical relationship between the timing of these two events.

Since the circulation generated by these flows comes from two sources, the boundary
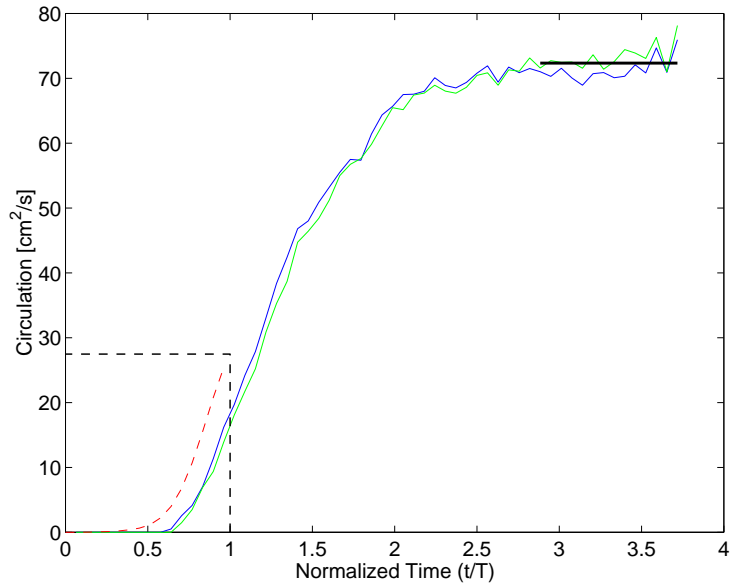
Figure 4.21: Circulation development for aspect ratio of 2. The solid curves are the clockwise and counterclockwise components. The dashed curve is the calculated momentum generated circulation. The solid horizontal line represents the value at which the circulation leveled out.
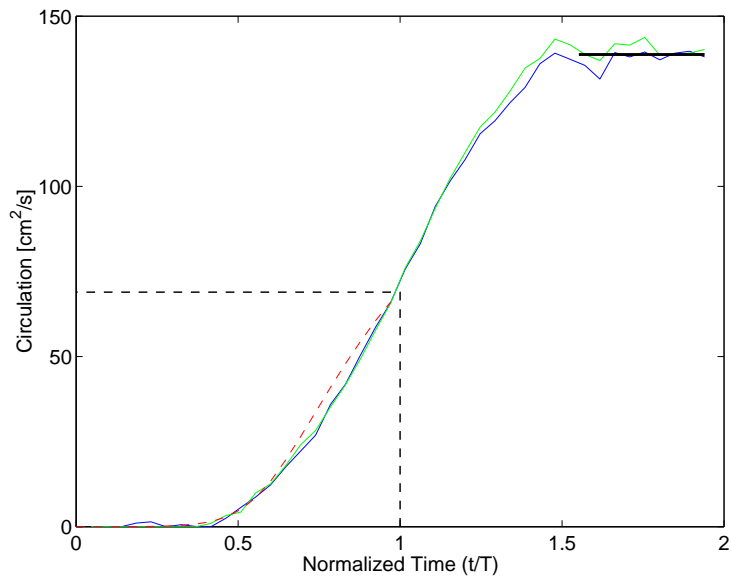

Figure 4.22: Circulation development for aspect ratio of 4. The solid curves are the clockwise and counterclockwise components. The dashed curve is the calculated momentum generated circulation. The solid horizontal line represents the value at which the circulation leveled out.
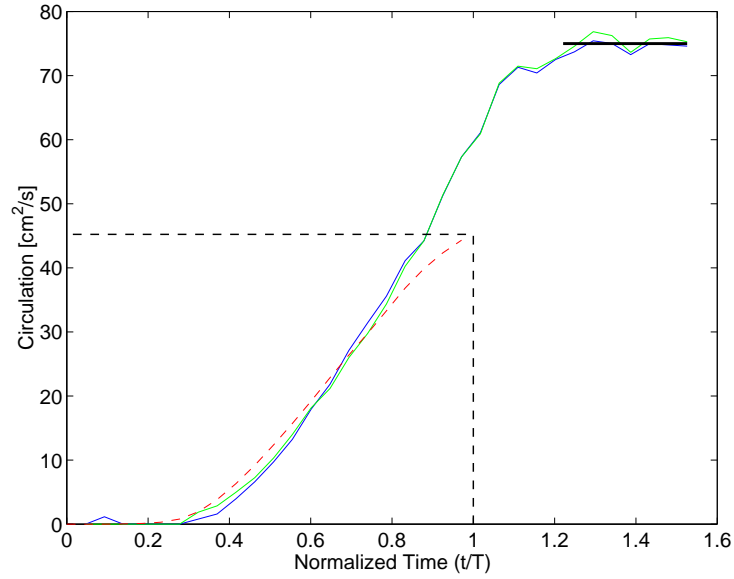
Figure 4.23: Circulation development for aspect ratio of 6. The solid curves are the clockwise and counterclockwise components. The dashed curve is the calculated momentum generated circulation. The solid horizontal line represents the value at which the circulation leveled out.
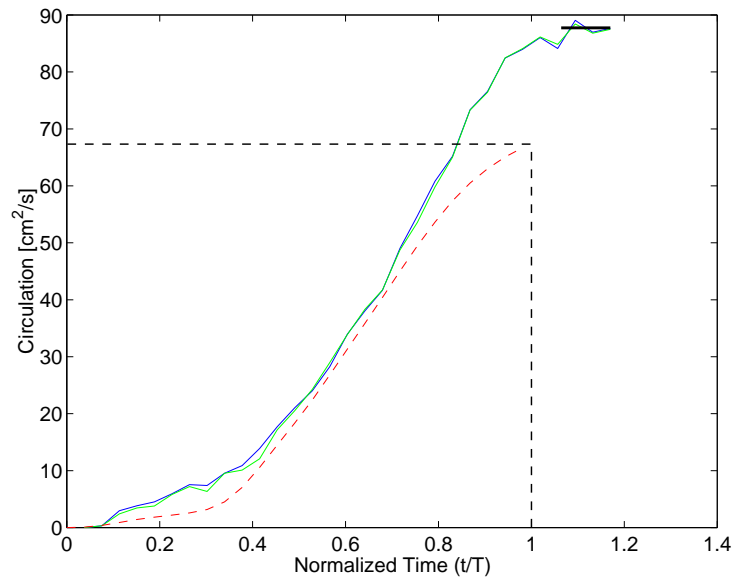

Figure 4.24: Circulation development for aspect ratio of 8. The solid curves are the clockwise and counterclockwise components. The dashed curve is the calculated momentum generated circulation. The solid horizontal line represents the value at which the circulation leveled out.

69

layer vorticity and buoyancy induced torques, an effort was made to determine the contribution from each. The circulation due to the boundary layer vorticity was estimated using the same method as in Chapter 3. The slug-flow model[8], previously shown mathematically in Eq. 3.7, is used as an initial estimate, and is corrected by the empirical relationship found by Didden[9] (Eq. 3.8). The complete formulation is shown here in Eq. 4.1.

$$\Gamma_{corr} = \left(1.14 + \frac{0.32}{L/D} \right) \int_0^T \frac{1}{2} U_e^2 dt \tag{4.1}$$

The difference in between the total circulation and the estimate of the circulation generated from the boundary layer vorticity was substantial in all cases, indicating that the circulation generated by baroclinic torques has a significant impact on the total circulation in the flow. Also, the total circulation for an aspect ratio of 8 increases faster than the estimated momentum generated circulation before the tube has discharged half of the fluid. For an aspect ratio of 4, the two curves were almost identical during the entire discharge period.

Figure 4.25 shows the total circulation developed as a function of the tube aspect ratio. It also shows the circulation generated by the boundary layer estimated by the method described above. Both of these values have been normalized by Γ^*, defined in Eq. 4.2. This is the circulation predicted by the slug-flow model for a tube with a constant exit velocity equal to the measured average velocity.

$$\Gamma^* = \frac{1}{2} \bar{U}^2 T = \frac{1}{2} \frac{\bar{U}^2 T^2}{T} = \frac{1}{2} \frac{L^2}{T} \tag{4.2}$$

Using the corrected slug flow model, and assuming a polynomial exit velocity profile, it can be shown that the circulation generated in the boundary layer would be a linear function of the aspect ratio. However, as seen in Fig. 2.2, the velocity profiles do not appear to be a family of polynomial curves. This would explain the non-linearity of the momentum generated circulation curve in Fig. 4.25.
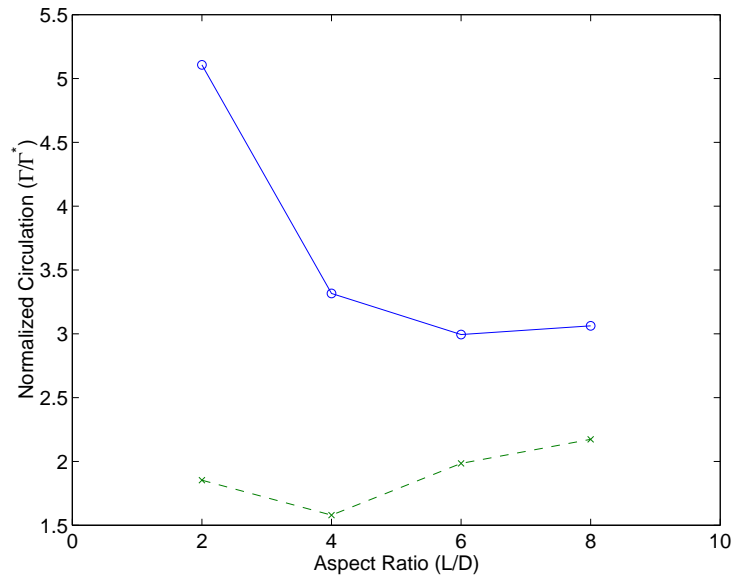
70

Figure 4.25: Final circulation value as a function of the tube aspect ratio. The solid curve represents the total circulation value averaged over the level portion of the curve. The dashed curve refers to the momentum generated circulation at the time the tube had completed drained of buoyant fluid.

Using the corrected slug flow model, the measured total circulation, and the measured exit velocity, the final circulation value can be divided into two portions. The first is the contribution due to the boundary layer, computed using the measured velocity profile according to Eq. 4.1. The second is the circulation generated by the action of the buoyant forces. Figure 4.26 shows this component plotted against the square root of the initial buoyant force. There is a clear linear relationship.

4.4.2 Impulse and Energy

The impulse of the flow was also investigated in light of changing aspect ratios. By computing the total impulse, assuming axisymmetric flow, and doing each "half" independently, it was possible to obtain some verification by comparing the results. The formulation used for the computation was discussed in the previous chapter. Also, Fig. 4.27 is included as a reference. This aspect ratio was discussed in Chapter 3.
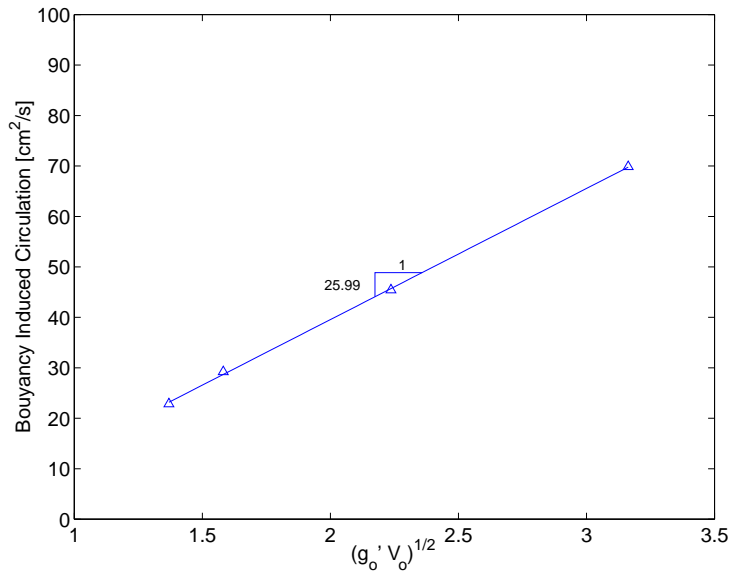
Figure 4.26: Circulation generated by buoyancy as a function of the square root of the initial buoyant force.

Shown in Figs. 4.28 to 4.30 are the results for the aspect ratios of $L/D = 4$, 6, and 8. The immediately interesting feature is the marked linear development after an initial period of very little increase. This slope can be interpreted as the total force acting over the entire flow field.

It was expected that the rate of change of the impulse, dI/dt, would be proportional to the initial buoyant force. Figure 4.31 shows a plot of the slopes of the previous figures against the initial buoyant force, $g_o'V_o$. The aspect ratios proceed in the order 6, 8, 2, and 4 since the larger aspect ratios have a smaller diameter and therefore volume.

The temporal development of the energy with time is included for completeness. The development is shown for the aspect ratios of $L/D = 4$, 6, and 8 in Figs. 4.33, 4.34, and 4.35. Initially there is a rapid increase with time, followed by a sharp transition to a nearly level region. This is qualitatively similar to the development seen in the circulation.
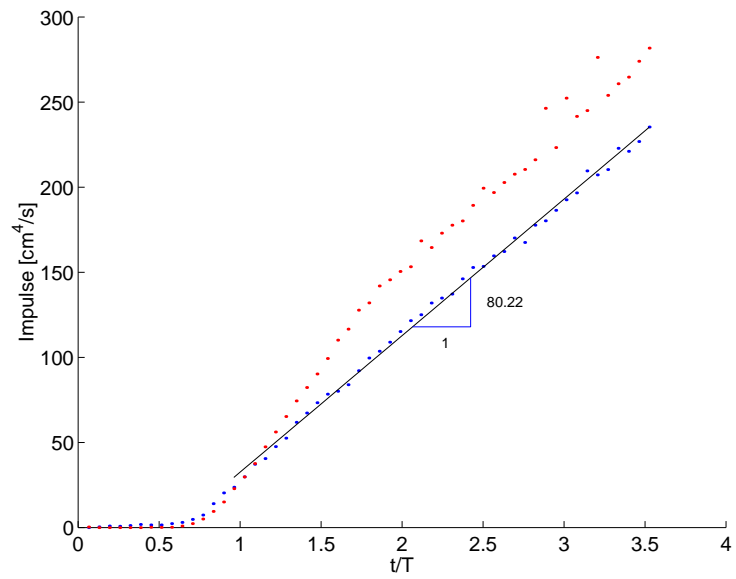
Figure 4.27: Temporal development of the impulse for $L/D = 2$. The dots represent individual field measurements and they are fitted by a straight line in the linear region.
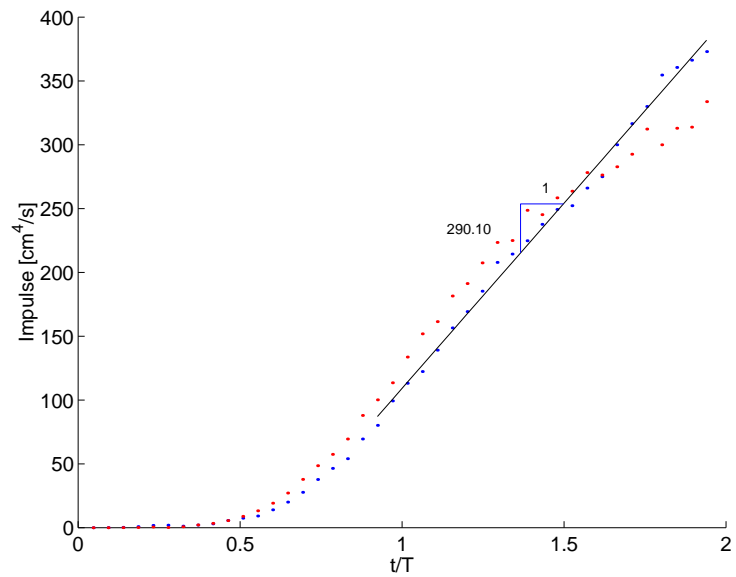

Figure 4.28: Temporal development of the impulse for $L/D = 4$. The dots represent individual field measurements and they are fitted by a straight line in the linear region.
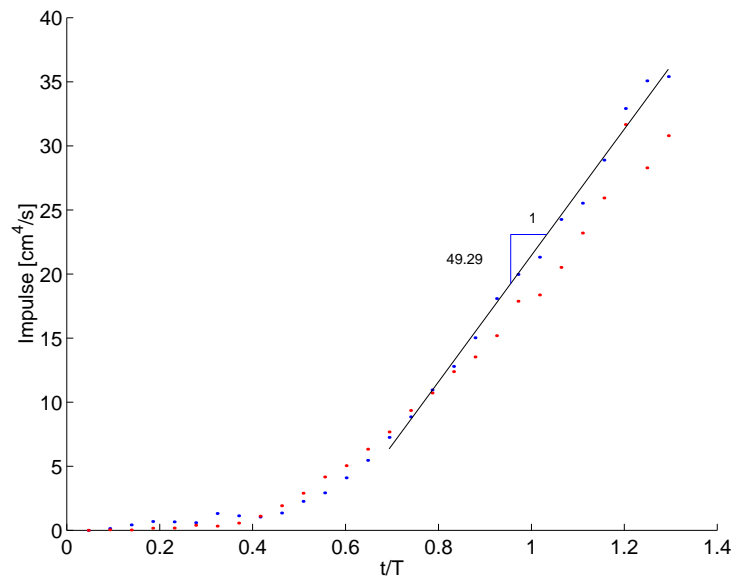
Figure 4.29: Temporal development of the impulse for $L/D = 6$. The dots represent individual field measurements and they are fitted by a straight line in the linear region.
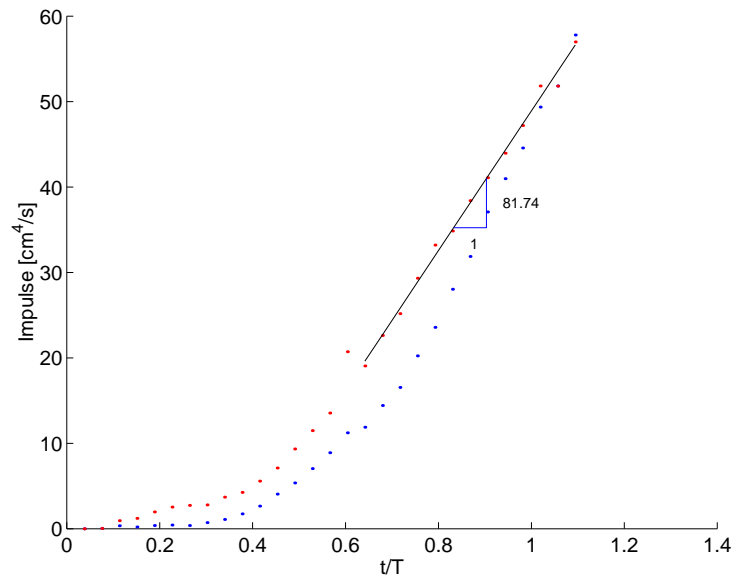

Figure 4.30: Temporal development of the impulse for $L/D = 8$. The dots represent individual field measurements and they are fitted by a straight line in the linear region.
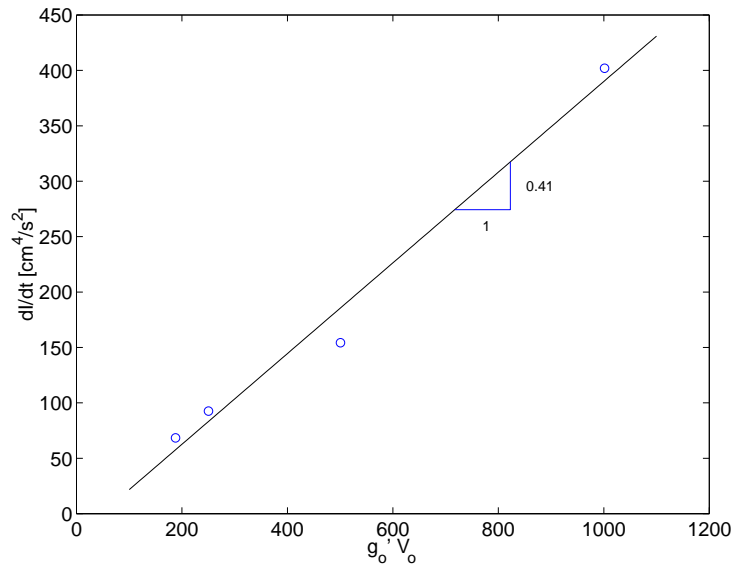
74

Figure 4.31: The rate of change of the impulse plotted against the initial total buoyant force.
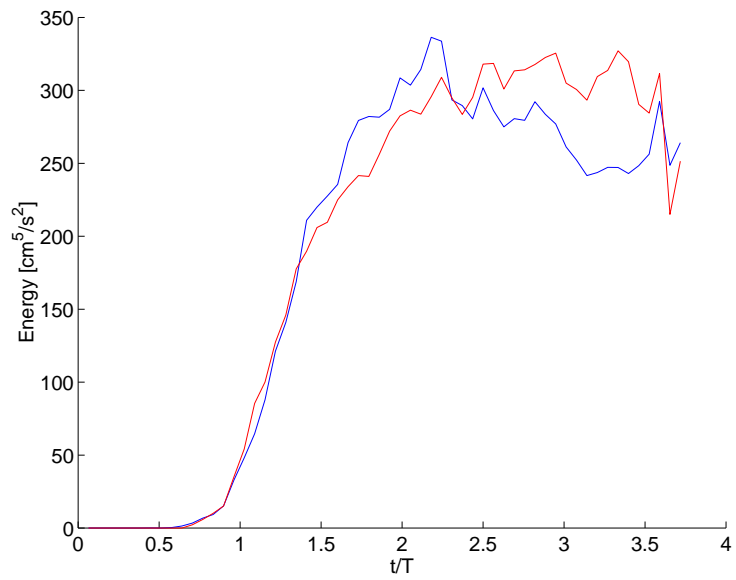

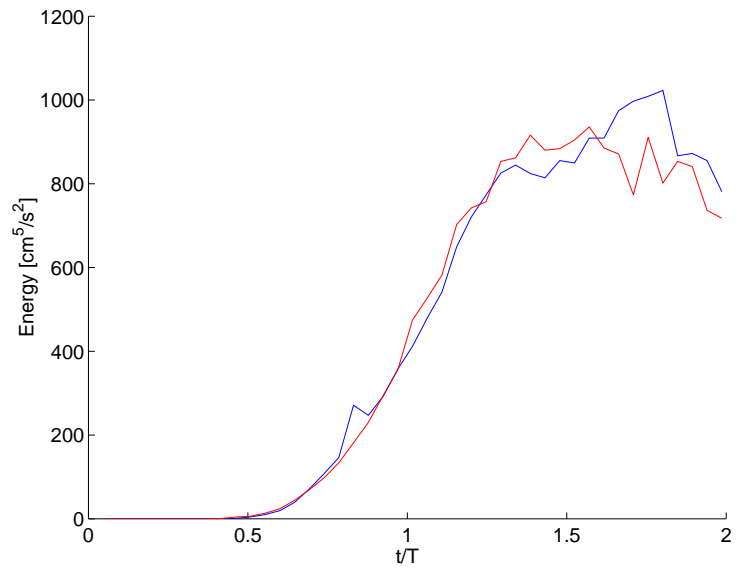Figure 4.32: Temporal development of the energy for $L/D = 2$.

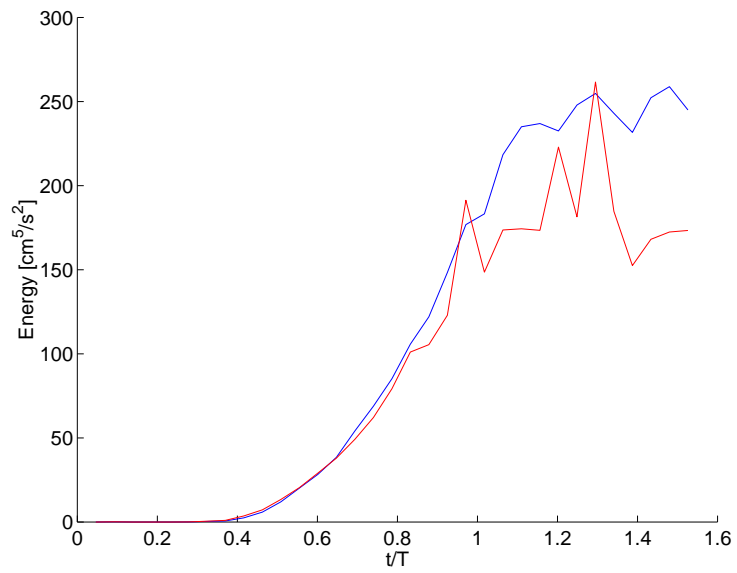Figure 4.33: Temporal development of the energy for $L/D = 4$.

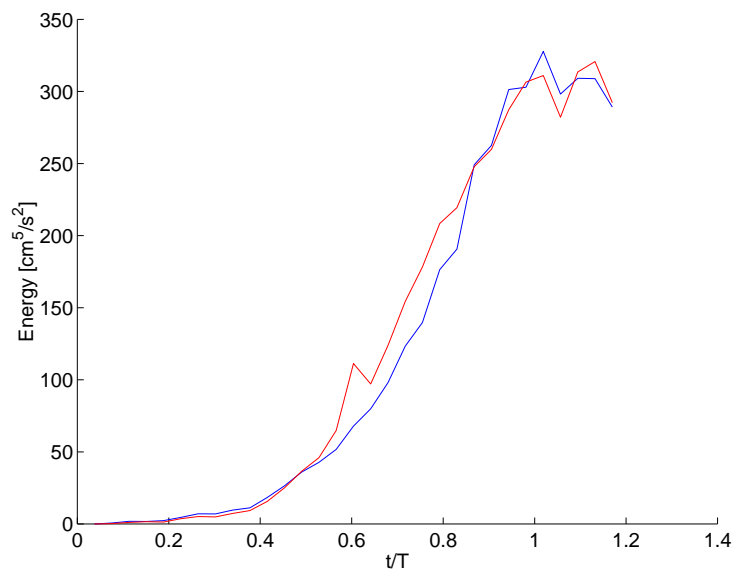Figure 4.34: Temporal development of the energy for $L/D = 6$.

Figure 4.35: Temporal development of the energy for $L/D = 8$.

5 Conclusions

The impact of buoyancy and initial fluid aspect ratio on the development of an axisymmetric starting flow has been investigated using both the PLIF and DPIV techniques. Aspect ratios of 2, 4, 6, and 8 were examined at a density difference of 4.7%. The results of the experiments can be grouped into two categories, the impact of buoyancy on vortex rings, and the impact of buoyancy on the leading vortex ring formation.

5.1   Vortex Rings

The addition of buoyancy to a simple vortex ring alters its behavior considerably. For a single vortex ring without buoyancy, the ring generally propagates at a nearly constant velocity when the viscous effects are small. Also, the ring diameter remains relatively constant. Both of these facts are a result of the low entrainment of ambient fluid by the ring structure. The addition of buoyancy causes the entrainment characteristics to change, thereby altering many of the features usually associated with a vortex ring. The major features of a buoyant vortex ring are as follows:

- The radius increases linearly with distance for $z/D > 2$

- Baroclinic torques generated most of the total circulation in the flow

- The impulse of the BVRncreases linearly with time

78

5.2   Aspect Ratio Effects

In light of work done on momentum driven starting jets, and the robustness of the model proposed by Gharib et al. in predicting the behavior in the near field, the effect of buoyancy on this model needed to be examined. There are several important points that have emerged from this research.

- The addition of buoyancy changes the nature of the starting flow

- The starting vortex ring is disrupted by buoyancy, and remains attached to the trailing flow

- The flow is divided into two phases, initial acceleration followed by a thermal like phase

- The distance to transition to the second phase is related to the cube root of the initial volume.

- The circulation generated by buoyancy is linearly related to the square root of the initial buoyant force

- The rate of change of the impulse is proportional to the initial buoyant force

5.3   Scope of the Results

Since the experiments were conducted with only one nozzle geometry, and the measurements were exclusively conducted in the near field, the sensitivity of the results to variations in the apparatus geometry may be questioned. However, the principle quantities measured, the circulation and impulse, are integral measures of the flow field. Extensive work has been done examining the effects of the nozzle geometry on the circulation in vortex ring generators [7, 9]. These experiments have indicated that the nozzle geometry only contributes secondarily to the amount of circulation generated, while the primary factor is the

aspect ratio of the ejected fluid column. Since the impulse is also an integrated measure, one may cautiously propose that it would also be less sensitive to the exact geometry of the generating apparatus.

5.4   Future Work

In order to more completely understand the impact of buoyancy on the development of the starting vortex ring, and the nature of the transition region, more experimental work needs to be done. Two regions need to be examined more closely. First, the flow field in the immediate vicinity of the generating tube should be examined at high resolution using the DPIV technique (velocity vector spacing < 0.05 D). This would help to understand the small scale structure seen in the PLIF images. Secondly, the transition region ($5 < z/D < 20$) needs to be examined using DPIV and PLIF. In this region, for the aspect ratio's examined, the flow changes to thermal like behavior. However, the current experiments did not include DPIV data for most of this region.

It would be desirable to control the exit velocity independently of the initial density difference. This may be possible for a range of Richardson numbers using a combination of the membrane with a driving piston.

References

[1] J. S. Turner. *Buoyancy effects in fluids*. Cambridge University Press, 1973.

[2] R. S. Scorer. Experiments on convection of isolated masses of buoyant fluid. *Journal of Fluid Mechanics*, 2:583–594, 1957.

[3] J. S. Turner. The starting plume in neutral surroundings. *Journal of Fluid Mechanics*, 13:356–368, 1962.

[4] H. Johari, Q. Zhang, M. Rose, and S. Bourque. Impulsively started turbulent jets. *AIAA Journal*, 35(4):657–662, 1997.

[5] S. C. Crow and F. H. Champagne. Orderly structure in jet turbulence. *Journal of Fluid Mechanics*, 48(3):547–591, 1971.

[6] C. E. Willert and M. Gharib. Digital particle image velocimetry. *Experiments in Fluids*, 10:181–193, 1991.

[7] M. Gharib, E. Rambod, and K. Shariff. A universal time scale for vortex ring formation. *Journal of Fluid Mechanics*, 360:121–140, 1998.

[8] K. Shariff and A. Leonard. Vortex rings. *Annual Review of Fluid Mechanics*, 24:235–279, 1992.

[9] N. Didden. On the formation of vortex rings: Rolling-up and production of circulation. *Journal of Applied Mathematics and Physics*, 30:101–116, 1979.

[10] H. Johari and M. Gharib. Near field development of starting buoyant flows. In *8th International Symposium on Flow Visualization*, 1998.

[11] A. Alahyari and E. K. Longmire. Particle image velocimetry in a variable density flow: application to a dynamically evolving microburst. *Experiments in Fluids*, 17:434–440, 1994.

[12] G. S. Rixon. The interaction of vortex generator jets with a turbulent boundary layer. Master's thesis, Worcester Polytechnic Institute, 2000.

[13] C. G. Koop and F. K. Browand. Instability and turbulence in a stratified fluid with shear. *Journal of Fluid Mechanics*, 93:135–159, 1979.

[14] P. G. Drazin and W. H. Reid. *Hydrodynamic Stability*. Cambridge University Press, 1981.

[15] D. M. Kuzo. *An Experimental Study of the Turbulent Transverse Jet*. PhD thesis, California Institute of Technology, 1995.

[16] B. Woodward. The motion in and around isolated thermals. *Q.J. Royal Meterological Society*, 85:144–151, 1957.

[17] B. M. Cetegen and J. C. Hermanson. Mixing characteristics of compressible vortex rings interacting with normal shock waves. *Combustion and Flame*, 100:232–240, 1995.